Alpha-radioimmunotherapy with At-211

Evaluation and imaging of normal tissues and tumors

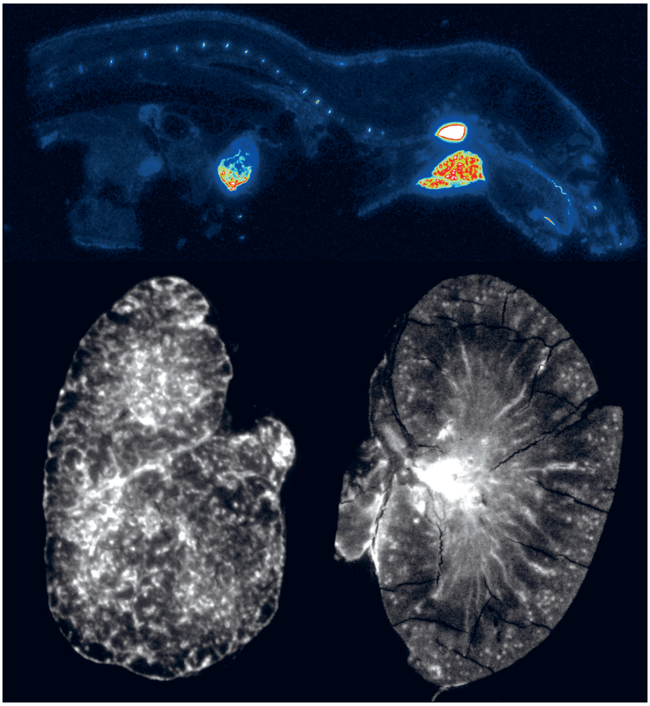

Tom Bäck

Institute of Clinical Sciences
at Sahlgrenska Academy
University of Gothenburg

UNIVERSITY OF GOTHENBURG

The Sahlgrenska Academy

Tom Bäck Alpha-radioimmunotherapy with At-211. Evaluation and imaging of normal tissues and tumors 2011

Alpha-radioimmunotherapy with At-211

Evaluation and imaging
of normal tissues and tumors

Tom Bäck

Department of Radiation Physics
Institute of Clinical Sciences at Sahlgrenska Academy
University of Gothenburg
Sweden

2011

Alpha-radioimmunotherapy with Astatine-211

Evaluation and imaging
of normal tissues and tumors

AKADEMISK AVHANDLING

som för avläggande av medicine doktorsexamen vid Sahlgrenska Akademin vid Göteborgs Universitet
kommer att offentligen försvaras i hörsal Arvid Carlsson, Medicinaregatan 3, Göteborg,
fredagen den 6 maj, 2011, kl. 13.00

av
Tom Bäck

Fakultetsopponent:

Professor George Sgouros
Radiology and Radiological Science
Johns Hopkins University, Baltimore, USA

Avhandlingen är baserad på följande delarbeten:

I.
Bäck T, Andersson H, Divgi CR, Hultborn R, Jensen H, Lindegren S, Palm S, Jacobsson L.
^{211}At radioimmunotherapy of subcutaneous human ovarian cancer xenografts: evaluation of relative biologic effectiveness of an alpha-emitter in vivo
J Nucl Med. 2005 Dec;46(12):2061-7.

II.
Bäck T, Haraldsson B, Hultborn R, Jensen H, Johansson ME, Lindegren S, Jacobsson L.
Glomerular filtration rate after alpha-radioimmunotherapy with ^{211}At-MX35-F(ab')$_2$: a long-term study of renal function in nude mice
Cancer Biother Radiopharm. 2009 Dec;24(6):649-58.

III.
Bäck, T and Jacobsson, L.
The α-Camera: A Quantitative Digital Autoradiography Technique Using a Charge-Coupled Device for Ex Vivo High-Resolution Bioimaging of α -Particles
J Nucl Med. 2010 Oct;51(10):1616-23.

Göteborg 2011

GÖTEBORGS UNIVERSITET

Doctoral Thesis, 2011
Department of Radiation Physics
Institute of Clinical Sciences at Sahlgrenska Academy
University of Gothenburg, Gothenburg
SE-413 45 Göteborg
SWEDEN

ISBN: 978-91-628-8293-8
E-publication: http://hdl.handle.net/2077/24500
Printed in Sweden by
Chalmers reproservice, Göteborg

The images on the front cover are α-camera images of cryosections that visualize the activity distribution of the α-emitting radionuclide ^{211}At in different mouse tissues. The top image shows the whole-body distribution 30 minutes after injection of free ^{211}At. The bottom images show the activity distribution of ^{211}At-MX35-F(Ab')$_2$ in a s.c. tumor (left) 6 hours after injection and of ^{211}At-Trastuzumab(IgG) in a kidney(right) 2 hours after injection.

ABSTRACT

Alpha-radioimmunotherapy (α-RIT) is an internal conformal radiotherapy of cancer using α-particle emitting radionuclides. Alpha-particles have a very short range in tissues (<100 μm) and a high linear energy transfer (LET), making them highly cytotoxic. Due to these characters α-emitters are potentially highly effective in eradication of small tumor cell clusters while at the same time toxicity of the adjacent normal tissue is avoided. Thus, α-RIT could be effective in treatment of cancers characterized by micrometastatic and minimal residual disease, e.g. ovarian and prostate cancer.

The biological effects of α-particles are grossly unknown and demand dedicated methodologies and evaluations for their interpretation. The aim was to evaluate the irradiation effects of the α-particle emitter ^{211}At for its use in α-RIT, using nude mice. This included studies on tumor efficacy, kidney toxicity and a study describing a novel bioimaging system, the α-camera, for assessment of radionuclide tissue distribution.

Growth inhibition (GI) after α-RIT with ^{211}At on s.c. OVCAR-3-tumors was compared with GI after external irradiation using ^{60}Co. For α-RIT, the mice were injected with ^{211}At-MX35-F(Ab')$_2$ at different activities. The GI was calculated for both irradiations and used to estimate the relative biological effectiveness (RBE) for α-RIT on tumors. At GI of 0.37, the RBE was found to be 4.8±0.7.

The long-term renal function after α-RIT was studied by measuring the glomerular filtration rate (GFR) after injection of ^{211}At-MX35-F(Ab')$_2$ at different activities. The GFR was measured repeatedly, using plasma clearance of ^{51}Cr-EDTA, up to 67 weeks after treatment. Dose-dependent and time-progressive reductions in GFR were found. For tumor-bearing mice, the kidney doses required for 50% reduction in GFR were 16±3.3 and 7.5±2.4 Gy at 8-30 and 31-67 weeks, respectively. For non-tumor-bearing mice the corresponding doses were 14±4.1 and 11.3±2.3 Gy. The maximum tolerable dose (MTD) to the kidneys (50% reduction in GFR) was 10 Gy.

A novel imaging system for ex vivo detection and quantification of α–emitters in tissues was developed, using an autoradiographic technique based on a scintillator and CCD for light detection. Initial evaluations of the imaging characteristics showed that the spatial resolution was 35 ±11 μm, the uniformity better than 2% and that the image pixel intensity was proportional to radioactivity in the imaged specimens. As examples of applications, the α-camera visualized and quantified differences in the tissue activity distributions after α-RIT with ^{211}At. For tumors, a very nonuniform distribution of ^{211}At-MX35-F(Ab')$_2$ was found from 10 mpi to 6 hpi. At 21 hpi the distribution was more uniform. Images of kidney-sections could identify the ^{211}At-distribution in different renal compartments. The 'cortex-to-whole-kidney-ratio' varied with time and bioconjugate size. The ^{211}At-MX35-F(Ab')$_2$ showed a marked retention in the renal cortex, corresponding to a ratio of 1.38±0.3 at 2 hpi.

The RBE found (4.8±0.7) gives further support for the use of α-particles in targeted radiotherapy. The MTD of 10 Gy suggests that the kidneys will not be the primary dose-limiting organ in α-RIT with ^{211}At. The α-camera will be an important tool for internal α-particle-dosimetry and for the development of α-RIT.

Keywords: astatine, alpha-particle, RBE, radioimmunotherapy, renal function, GFR, imaging, targeted alpha therapy

LIST OF PAPERS

I.

Bäck T, Andersson H, Divgi CR, Hultborn R, Jensen H, Lindegren S, Palm S, Jacobsson L.
^{211}At radioimmunotherapy of subcutaneous human ovarian cancer xenografts: evaluation of relative biologic effectiveness of an alpha-emitter in vivo.
J Nucl Med. 2005 Dec;46(12):2061-7.

II.

Bäck T, Haraldsson B, Hultborn R, Jensen H, Johansson ME, Lindegren S, Jacobsson L.
Glomerular filtration rate after alpha-radioimmunotherapy with ^{211}At-MX35-F(ab')$_2$: a long-term study of renal function in nude mice.
Cancer Biother Radiopharm. 2009 Dec;24(6):649-58.

III.

Bäck, T and Jacobsson, L.
The α-Camera: A Quantitative Digital Autoradiography Technique Using a Charge-Coupled Device for Ex Vivo High-Resolution Bioimaging of α-Particles.
J Nucl Med. 2010 Oct;51(10):1616-23.

CONTENTS

ABBREVATIONS

α-RIT	alpha-radioimmunotherapy
CCD	charge-coupled device
DNA	deoxyribonucleic acid
DSB	double strand breaks
EDTA	ethylenediaminetetraacetic acid
eGFR	estimated glomerular filtration rate
FWHM	full width at half maximum
GI	growth inhibition
GFR	glomerular filtration rate
hpi	hours post injection
i.v.	intravenous
MAb	monoclonal antibody
MDS	multiply damaged sites
mpi	minutes post injection
MTA	maximum tolerable activity
MTD	maximum tolerable absorbed dose
LET	linear energy transfer
RBE	relative biological effectiveness
RIT	radioimmunotherapy
ROI	region of interest
RT	radiotherapy
s.c.	subcutaneous
SE-radius	Stokes-Einstein radius
SF	surviving fraction
SNR	signal-to-noise ratio
SSB	single strand breaks
TCP	tumor cure probability

1. INTRODUCTION

Radioimmunotherapy (RIT) is an internal radiation cancer treatment using ionizing radiation to kill cancer cells. The treatment is often called targeted radiotherapy because it is aimed at specifically target and irradiating the cancer cells with the radiation source, a radioactive agent. The targeting agent in RIT is an antibody molecule directed to specific antigenic sites localized on the membrane of cancer cells. An antibody recognizes and binds to the antigen through the antigenic determinant; a specific part of the antigen called the epitope. The antigenic sites and its epitopes can be specifically expressed, or over-expressed, on cancer cells and thereby used as targets. By chemical conjugation, the antibody molecule is labeled to carry an unstable element, radionuclide, which upon decay emits radiation. After administration in the human body, the radiolabeled antibody is supposed to carry the radionuclide to the tumor sites, so that the radiation energy is deposited on, inside or in the close vicinity of the cancer cells.

1.1 Radioimmunotherapy

The use of antibodies as targeting agents for cancer started in the 1950s, when Pressman and Korngold [1, 2] showed that anti-tumor sera could be produced in rabbits by injecting tumor sediment or cells. They found that the radioiodinated globulin fraction of the antisera contained antibodies that, after injection in tumor-bearing mice or rats, could target and localize to a greater extent in tumors, than in normal tissues like liver, kidney and lungs. Apart from showing the presence of tumor-localizing antibodies in anti-tumor sera, these studies showed how injected radioactivity carried by antibodies could be targeted to tumors, and so laid the foundation of RIT. Pressman and co-workers [3] continued their work by studying the characteristics and properties of the antigen, or antigenic materials, which were responsible for the observed in vivo localization. More than half-a-century later, the research efforts devoted to seek possible cancer targets is still expanding and by use of modern molecular technology a vast number of cellular antigens or receptors have been identified. The next crucial step to the development of antibody-based therapy was taken in

1975 by Köhler and Milstein [4, 5] when they reported that it was possible to immortalize antibody-producing cells and that these hybridized cells could be grown *in vitro* in large cultures to provide antibodies directed against a specific immunogen. Early pilot experimental studies of radioimmunodetection and therapy were conducted e.g. by Goldenberg et al. [6-8] starting in the late 1970s. In 1980, Nadler and co-workers [9-11] performed the first human immunotherapy treatment in the United States, using a monoclonal antibody developed against a tumor-associated antigen (B-lymphocyte specific) from tumor cells of a patient with B-cell lymphoma. Although their study utilized an unlabeled antibody, they concluded that one of the potential uses of monoclonal antibodies is the delivery of cytotoxic agents [11]. This conclusion, envisioning RIT, should in fact turn to be proven true for the same type of cancer (lymphoma) 20 years later. After extensive pre-clinical studies with promising results, the US Food and Drug Administration in 2002 approved the first two drugs for RIT of non-Hodgkin's lymphoma, Zevalin (^{90}Y) [12] and Bexxar (^{131}I) [13].

The progress made for RIT to gain a role in the treatment of cancer has relied on the use of β-emitters to deliver the cytotoxic effects of ionizing radiation. Several reviews [14-18] describe the development of RIT and the vast number of studies that laid the foundation. Three commonly used radionuclides have been ^{90}Y, ^{131}I and ^{177}Lu. The β-particles of their emissions have mean ranges in tissue of 4.3, 0.4 and 0.25 mm, respectively [19], in relation to their energies. Mathematical models have been used to show that each β-emitter has an optimal tumor size range for potential tumor cure. If the radionuclide is distributed uniformly within the tumor, the optimal tumor size will depend on the range of the emitted particles. O'Donoghue *et al*. [20] estimated that the optimal tumor diameters for cure were 34, 3.4 and 2 mm for ^{90}Y, ^{131}I and ^{177}Lu, respectively. Thus, shorter particle range corresponds to a smaller optimal cure diameter. The reason for this is that when the tumors are small compared to the range of the emissions, a larger fraction of the β-particles will escape the target volume and deposit their energy outside of the tumor. The fraction of energy absorbed (from uniform sources within the target) in the target will be higher for shorter ranged than for longer ranged particles and also higher for bigger sized tumor than for smaller, as shown by Siegel and Stabin [21]. An important factor that should be weighed into the considerations above is the so called 'cross-fire' effect. This refers to the situation where non-targeted cells are irradiated by particles that are emitted from neighboring targeted cells. This effect will increase with increasing particle range and it may contribute both positively and negatively to a therapeutic outcome. It may be beneficial to compensate for nonuniform activity distributions that arise from e.g. nonuniform antibody distribution due to heterogeneous antigen expression or variations in tumor vascularization. But 'cross-fire' will also contribute to irradiation of the normal cells that are located near the tumor nodules. The different clinical circumstances will have to determine the choice of radionuclide and the best choice may prove to be a combination, as expressed by many authors e.g. Oliver Press [22], one of the endeavourers in the establishment of RIT.

Returning to the 1950s, Pressman and Korngold noted in their early studies that their radio-iodinated antibodies also localized in, and carried radioactivity to, normal organs. More than half a century later, this is still the major factor preventing RIT from being a successful method of treating cancer. Although the idea of using monoclonal antibodies as 'magic bullets' to seek out invading tumor cells, initially envisioned by Paul Ehrlich [23-25], has been realized through the development of clinical therapies for certain cancers, there are still many limitations on the use of RIT for the treatment of cancer. The amount of radioactivity that can be administered to patients today is limited by the uptake of radioactivity in normal tissues (usually the bone marrow), thus limiting the absorbed dose to a tumor.

1.2 Alpha-radioimmunotherapy

The rationale for using α-emitting radionuclides in RIT is the physical characters of the α-particles: a very short range in tissue (<100 μm) and a very high energy that makes them highly potent in killing cells. These features mean that α-radioimmunotherapy (α-RIT) could be well suited for cancers characterized by the presence of single tumor cells up to small tumor clusters. This includes treatment of cancers present in the circulation such as lymphoma and leukemia, micrometastatic and minimal residual diseases, and malignancies characterized by tumor cells or small clusters floating free or growing on compartment walls or on the lining of various cavities, e.g. the peritoneal surface. For such diseases, the use of α-particles could potentially eradicate the tumor cells while at the same time avoid toxicity of the adjacent normal tissue. One such disease is ovarian cancer which is characterized by remaining micrometastatic disease in the abdominal cavity. Ovarian cancer has been the main focus for our research group in Gothenburg. A large number of pre-clinical studies [26-34] have shown that α-RIT with ^{211}At-MX35-F(ab')$_2$ is a safe and effective intraperitoneal therapy of micrometastatic ovarian cancer and that this treatment might be beneficial as a consolidating treatment of women suffering from ovarian carcinoma. The treatment will be best suited for patients in certain stages, i.e. women who after a primary cytoreductive surgery followed by chemotherapy show a complete clinical remission, but are at the risk of having residual small tumors and clusters of cells (less than 0.5 mm). With the support of the promising pre-clinical results a clinical trial (Phase I) has been carried out in Gothenburg, with the purpose of evaluating toxicity and dosimetry [35]. Nine women were included in the first part (2005-2009) and in a second part (2009-2011) another 3 patients were included at levels of administered activity that were escalated to levels presumed for a future clinical therapy. It could be concluded from the study that no toxicity was found at levels of activity that should be therapeutic for the micrometastases, according to pre-clinical dose estimations [30].

Despite the appeal of the concept, the use of α-particle emitters in internal radiotherapy (RT) is still in its infancy. In part, this is due to the limited radionuclide availability. But the interest in α-emitters is expanding and there is a growing number of preclinical studies, some of which have led the way to a few clinical trials. Three α-emitting radionuclides have been used clinically in phase I studies of α-RIT of cancer, ^{211}At, ^{213}Bi and ^{225}Ac. Bismuth-213 [36, 37] and ^{225}Ac [38] have been used in humans for treatment of leukemia. Astatine-211 has been used for brain cancer [39] and recently also, as mentioned above, for the treatment of ovarian cancer by our group in Gothenburg [35]. In addition to this, ^{223}Ra ($RaCl_3$) has been investigated for treatment of bone metastases in prostate cancer [40].

1.3 Aims of the thesis

The primary aim of this thesis was to further evaluate the irradiation effects of the α-particle emitter ^{211}At in some aspects, important for its use in α-RIT of cancer. Despite the growing interest for α-emitters in RIT, the biological effects from α-particles in this setting are grossly unknown. Many studies have shown promising results, indicating that internal RT with α-emitters could be an effective therapy for cancers that would be difficult or even impossible to treat by other means. The development and implementation of targeted α-therapy will rely on the relation between tumor efficacy and normal tissue toxicity. The first two studies of this thesis evaluate the effects of α-RIT with ^{211}At on tumors (Paper I) and on kidneys (Paper II). The unique characters of α-particles (high cytotoxicity and short path length), demand dedicated evaluations and methodologies for the interpretation of their biological effects related to dosimetry. Paper III describes a novel α-imaging technique that may become one of the tools needed for the understanding and development of targeted α-therapy. All studies were conducted in experimental animal designs, using immunodeficient nude mice, with permission from the Ethics Committee for Animal Experiments of the University of Gothenburg.

Internal radiotherapy exploiting α-emitters is an interdisciplinary field of research its development depends on theoretical and experimental knowledge from a variety of competence areas. The comprehensive summary of this compilation thesis was written with the primary aim of introducing a reader, entering the field of research, in some basic perspectives but also to discuss selected perspectives that are of special importance in the three papers. As a consequence of this, I have chosen not to include a detailed description of the ‘materials and methods’ from each paper, instead the reader is referred to Paper I-III.

Specific aim of Paper I

The study reported in Paper I was carried out to study the *in vivo* effect of internal α-RIT with ^{211}At-MX35-F(ab')$_2$, as compared to external ^{60}Co γ-irradiation, on tumor growth of s.c. xenografts of the human ovarian cancer cell line OVCAR-3. The specific aim was to estimate the relative biological effectiveness (RBE) of α-RIT with ^{211}At, using a clinical relevant endpoint and external ^{60}Co-irradiation as the reference, in an *in vivo* model of tumor growth inhibition.

Specific aim of Paper II

The study reported in Paper II aimed at evaluating the acute and long-term radiation effects on the kidneys after α-RIT with ^{211}At-MX35-F(ab')$_2$. The specific aim was to estimate the reduction in renal function after α-RIT over time, by serial measurements of glomerular filtration rate (GFR) up to 67 weeks after therapy.

Specific aim of Paper III

Paper III describes the development of a novel imaging technology, the α-camera, dedicated for the *ex vivo* detection and quantification of α-particles in tissues. The specific aims of this study were to evaluate the important characteristics of this imaging system and to exemplify some of its applications in the development of α-RIT.

2. BACKGROUND

2.1 Alpha-particle emitting radionuclides

The α-emitting radionuclides are unstable elements that upon decay undergo a transformation of the atomic nucleus. In this transformation, the radionuclide releases its excess energy by emitting a so called α-particle. Originating from the nucleus of the radionuclide, the α-particle consists of two protons and two neutrons and so corresponds to a nucleus of the element helium ^{4}He, but lacking two electrons. Thus, an α-particle is a heavy weight and charged (+2) particle.

The decay of α-emitting radionuclides can also involve other decay modes, so that the emission can include photons (X-ray or γ) and β-particles. These emissions can be important by making possible *in vivo*-imaging of the radionuclide or by allowing radioactivity detection and activity measurement using standard isotope laboratory equipment like isotope calibrator, γ-counter or detectors used for radiation protection.

2.2 Astatine-211

2.2.1 Decay

The half-life ($T_{½}$) of ^{211}At is 7.21 h and the decay has two branches, both of which involve the emission of an α-particle. Either it can decay (58.3% probability) to form the daughter nuclide ^{207}Bi. This branch can be described by the simplified scheme:

$$(1) \qquad {}^{211}_{85}\mathrm{At} \rightarrow {}^{207}_{83}\mathrm{Bi} + {}^{4}_{2}\mathrm{He} \quad [\alpha, 5.87\ \mathrm{MeV}]$$

In the other branch (42.7% probability), ^{211}At first decays to form the daughter ^{211}Po that in turn decays ($T_{½}$ = 0.52 s) to form ^{207}Pb, and can be described as:

$$(2) \qquad {}^{211}_{85}\mathrm{At} \rightarrow {}^{211}_{84}\mathrm{Po} \rightarrow {}^{207}_{82}\mathrm{Pb} + {}^{4}_{2}\mathrm{He} \quad [\alpha, 7.45\ \mathrm{MeV}]$$

The daughter ^{207}Bi ($T_{½}$ = 38 y) of the first branch (1) decays to form ^{207}Pb (same as in branch 2), which a stable element. The decay of ^{211}At to ^{211}Po in (2) is by electron capture and involves the emission of X-ray photons (77-92 keV).

2.2.2 Production

The production of ^{211}At for experimental purposes is done by use of a cyclotron. This a done by the nuclear reaction ^{209}Bi(α,2n)^{211}At. Alpha-particles are accelerated to high energies in the cyclotron and bombarded on a ^{209}Bi-target. This reaction can be described as:

$${}^{4}_{2}\mathrm{He} \quad [\alpha, \sim 28\ \mathrm{MeV}] \ + \ {}^{209}_{83}\mathrm{Bi} \rightarrow {}^{211}_{85}\mathrm{At} \ + \ 2\ \mathrm{neutrons}$$

The ^{211}At used in the studies of this thesis was produced at the PET & Cyclotron Unit, Rigshospitalet, Denmark.

2.2.3 Distillation

The produced ^{211}At has to be isolated from the cyclotron target and in the studies of this thesis this was performed by a dry distillation procedure initially described by Wilbur *et al.* [41] and later refined by Lindegren *et al.* [42]. In short, the solid bismuth layer was mechanically removed from the irradiated target and placed in quartz glass tube still that was heated by a furnace. At a temperature of 670°C the ^{211}At was evaporated and evacuated from the glass still into a capillary tube by reduced pressure. The capillary tube was pre-cooled to -77°C, so that evaporated ^{211}At was trapped in the capillary tube by condensation. Finally, the ^{211}At was transferred to a glass vial by rinsing the capillary tube with chloroform. Prior to labeling procedures, the chloroform was evaporated so that the ^{211}At could be resolved in a suitable solution or buffer.

2.2.4 Radiolabeling

The radiolabeling of the antibodies with ^{211}At was performed in a two-step single-pot reaction. In the first step, an intermediate labeling reagent was labeled with ^{211}At. After evaporating the solvent of the labeling mixture, the conjugation of the antibody was performed in a second step by adding the antibody to the crude residue of the labeling mixture. Finally, the labeled antibody fraction was isolated by a liquid chromatography method. The radiolabeling procedure of ^{211}At has been described in detail [43], and also further developed [44], by Lindegren *et al*.

2.3 The radiobiological effects of α-particles

Alpha particles are heavy weight charged particles (2+) that once emitted possess a kinetic energy in the range of e.g. 5-7 MeV. Because of the heavy weight, their speed will be relatively slow (i.e. relative to the high-speed e^-) which results in a high probability of energy transfers. This way, a linear high density ionization track is formed that in water is shorter than 100 μm. The transfer of energy can be described by the mean linear transfer of energy (LET) along the track. The LET for α-particles is high, around 80-100 keV/μm, while for β-particles and electrons generated from x-rays or γ-rays the LET is low (a few keV/μm). At the end of a α-particle-track the rate of energy deposited can increase to ~300 keV/μm. The mean LET for the α-particles emitted by ^{211}At (5.87 MeV and 7.45 MeV) is 122 and 106 keV/μm and correspond to a maximum range in tissue of 48 and 71 μm, respectively.

The effect of ionizing radiation on living cells is dependent on the LET. Radiation causes cell kill through ionizations or excitations of molecular atoms. These effects can be induced directly or indirectly. For α-particles the direct effect dominates, and the particles interact directly by ionizing atoms in cellular molecules, e.g. DNA. Direct ionization of the DNA can cause so-called double strand breaks (DSB) or multiply damaged sites (MDS) which are more difficult for the cell to repair. In comparison to more sparsely ionizing low-LET radiation, high-LET radiation has a high probability of producing lethal DNA-damages through irreparable DSB. Radiation can also cause cellular damage by indirect action. This takes place when atoms of other molecules become ionized, e.g. H_2O which is the most frequent molecule in cells and their nuclei. This produces reactive free radicals, which in spite of short half-life can reach the DNA by diffusion and cause a variety of lesions (e.g. SSB) by breakage of chemical bonds. Two thirds of the biological damage caused by low-LET radiation is the result of indirect action, and a large proportion of this damage is repairable, i.e. it is sub-lethal. The densely ionizing radiation of α-particles causes a larger proportion of irreparable damage.

2.4 Cell survival

The effect of radiation on cell survival can be studied *in vitro* in different cell assays, where cell survival after irradiation is studied at different levels of absorbed radiation dose. Typically, cell survival curves are generated by plotting the surviving fraction of cells (SF) versus absorbed dose. Different models can be used to represent the shape of the cell survival curves. For the high-LET radiation of α-particles it has been observed that the logarithm of cell survival is a straight line when plotted versus absorbed dose (D), i.e. survival is an exponential function of dose and can be described with the model:

$$SF = e^{-\alpha D}$$

where the survival curve can be described by just one parameter, the α. This parameter is a measure of radiosensitivity of the cells. The parameter D_0 is the dose required to reduce the average survival from 1 to 0.37 (e^{-1}) and the parameter α is equal to $1/D_0$. For single high-dose-rate exposure with low-LET radiation (e.g. photons or β-particles), after an initial linear slope, the log survival curve has a bending shape and the commonly used model to represent the cell survival is the linear-quadratic (LQ)-model:

$$SF = e^{-\alpha D - \beta D^2}$$

In this model a second component of cell killing is introduced), βD^2 (proportional to the square of the absorbed dose) and this term is interpreted to represent accumulated and repairable damages (sub-lethal) from double-hit effects. The LQ-model has been extended to be used also in protracted and low-dose-rate irradiations like targeted radionuclide therapy using β-emitters [45, 46].

2.5 Effects of radiation on tissue

The general consensus is that the cell nucleus is the critical target for radiation and that cell death, induced by irreparable damages to the DNA, will mainly occur in mitosis when the cells try to divide. The time from radiation exposure to cell death will therefore depend on the turnover rate of the irradiated cells. The time-scale on which the biological effects of radiation are manifested at the tissue level is broad and the effects are usually divided in early (acute) and late effects. Early reactions can occur days to weeks after irradiation, while late effects (e.g. fibrosis, cancer induction and heritable effects) can occur after years to several decades. In radiotherapy, the tissues are usually divided into early or late responding tissues. Both physical parameters (e.g. dose, dose rate and fractionation schedule) and biological features (e.g. intrinsic radiosensitivity and rate of cellular turnover) will affect the extent and delay of the observed effects. For early responding tissues (like epithelial and hematopoietic tissue as well as most tumors) the population of cells is more heterogeneous, having a larger fraction of cells actively cycling. For late responding tissues (like vascular or mesenchymal tissue), only a small fraction of the cells are cycling and the tissue represent a more homogeneous cell population with most of the cells in a resting phase. When the resting cells eventually are triggered to undergo mitosis, the damages are identified, and the cells succumb. The early reactions often are transient and gradually resolved after treatment. Late effects, on the other hand, often tend to be irreversible and progressive. In recent years, the paradigm of DNA as the sole radiation target has been revised by findings supporting a role for extranuclear targets and signaling from hit to non-hit cells. Several reviews describe the new and expanding knowledge in radiation biology [47-49].

2.6 Dosimetry of Astatine-211

2.6.1 Different methods for dosimetry of α-particles

One of the major impediments to targeted radiotherapy is the heterogeneous distributions of the targeting agents in tumors and normal tissues. In the use of internal α-emitters, the consequences of heterogeneous targeting are of special importance due to the short path length of the α-particles. Variations in activity distribution within a tissue can result in large variations in absorbed dose between different cells within the same tissue. This poses strong challenges on the methods needed for relevant dosimetry. In principle, the scale for which the absorbed dose from particle emitters (α & β) needs to be determined corresponds to the range of the particles. The scale needed for β-emitters is within the range of millimeters, while for α-particles a scale of micrometers can be needed [50]. It is important to note that a nonuniform dose distribution will require a higher absorbed dose, for the same survival or cell kill, than when the dose is distributed uniformly. As described early by Humm *et al.* [51], the dose-response curve for a nonuniform α-particle irradiation may depart significantly from the typical monoexponential curve. The difference in cell survival from uniform versus nonuniform distribution can be more pronounced for cells of higher radiosensitivity [52].

As outlined by Sgouros [53] and recently by the MIRD committee [54], dosimetry of α-particles in targeted radiotherapy can be performed by three different approaches; microdosimetry, cell-level dosimetry or organ-level dosimetry. Microdosimetry addresses the fact that the deposition of energy in cells from radiation in small targets is a random process that may lead to cell death and that the effects are stochastic in nature. For α-particles and the situations where only a few events contributes to the total dose, e.g. one hit of a single cell nucleus, the variations in absorbed dose (specific energy) to the nucleus can be very large [55]. The specific energy for one hit will depend on factors like distance from the spatial location of the α-particle-emission to the cell nucleus, diameter of the nucleus and track length through nucleus. Microdosimetry estimates absorbed dose (specific energy) in terms of probabilities and require precise knowledge on source-to-targets geometries and dimensions. Such knowledge exists only in theoretical models of idealized geometry or *in vitro* experiments of cell survival and this is where microdosimetry have been developed and used [50, 55-61]. For situations where a high mean absorbed to the cells is the result of many events, c ell-level dosimetry can be used [53]. In this approach, the different cell compartments (e.g. cell surface, cytoplasm or nucleus) are assumed to have a uniform distribution of the radionuclide. The absorbed dose to a target volume can be calculated from the total number of decays in a corresponding source region (e.g. cytoplasm → nucleus) by help of a factor, the S value, which consider the fraction of energy of the source-decays that is absorbed in the target volume. The S value will depend on the geometrical dimensions and the particle energies. A list of cellular S values for α-particle has been published [62] that can assist cell-level dosimetry calculation. For targeted α-therapy, the relevant effects that need to be predicted from dosimetry are the more acute deterministic effects (tumor efficacy or normal tissue impairment) rather than late stochastic effects (e.g. cancer induction). Organ-level dosimetry is described in the next section.

2.6.2 Dosimetry method in Paper I and II

The dosimetry method used in Paper I and II was by the organ-level approach with estimation of the mean absorbed dose to the whole tumor or the whole kidney. After administration of ^{211}At-MX35-F(ab')$_{2,}$ the activity uptake in the tissue at different times postinjection was measured using a γ-counter. The mean values of tissue uptake (% injected activity/g tissue) were used to calculate the cumulated activity concentration, $\tilde{C}$ (total number of decays/kg), in the tissue. This was done by calculating the area-under-curve of a plot of the tissue uptake versus time (from zero to 48 hours). The mean absorbed dose, D, to the tissue was calculated using the formula:

$$D = \tilde{C} \cdot \Delta \cdot \emptyset$$

The mean energy emitted per ^{211}At decay (Δ) used was $1.09 \cdot 10^{-12}$ J/decay and this energy was for the α-particles only (i.e. contribution from the photons and electrons were neglected). It was assumed that all α-particles from decays within one tissue deposited all their energy within this tissue only (and no contribution from surrounding tissues), so the absorbed fraction, $\emptyset$, was set to 1.

2.7 Normal tissue versus tumors – the therapeutic window

When using ionizing radiation in the treatment of cancer the aim is to kill the tumor cells, while sparing the cells of normal tissues. In the case of internal irradiation, except for some loco-regional treatments, the blood is acting as a medium in which the radiation-carrying substances are transported to the cancer cells. In this transport, during which the radionuclide decays and emits radiation, cells of the normal tissues will be irradiated. In fact, each tissue or organ, including tumors, has its own dynamic phases of uptake, retention and release of the radionuclide. This is easily understood from the typical scenario in internal RT: a tumor seeking substance (carrying a radionuclide) is injected in the blood stream with the purpose to target cancer cells. Following the blood stream, the radionuclide immediately passes several major organs like the heart, kidneys, lungs, liver, bone marrow etc. When using the α-emitting radionuclide ^{211}At, the absorbed fraction can be assumed to be 1 and the dose contribution other than from α-particles can be neglected (as described above). Thus, in each of these organs, it is the radioactivity content over time that leads to a certain total absorbed dose from radiation for that organ. What limits the amount of activity that can be administered in cancer treatment with internal radiotherapy, and thereby limits the absorbed dose to the tumor, is the content of radioactivity in normal tissues (most often the bone marrow). Because of this, important knowledge is needed prior to therapy:

a. Which normal tissue will be the primary dose limiting organ?
b. What is the maximum tolerable absorbed dose (MTD) for that organ?
c. What is the maximum tolerable activity (MTA) corresponding to the MTD?
d. Does the MTA correspond to a therapeutic absorbed dose to the tumor?

The administered activity will in turn decide what absorbed dose can be achieved to the tumor. This situation can be exemplified by combining the dose-effect data presented in

Paper I and II of this thesis. In these studies, the activity uptake of the radionuclide in the tumor (Paper I) and in the kidneys (Paper II) after injection of ^{211}At-MX35-F(ab')$_2$ was measured over time. The uptake data were used to estimate a mean absorbed dose to the tumors and organs and for a certain administered activity, expressed as Gy per MBq. In both studies, the radiation effect on the respective tissues was measured at different levels of absorbed dose, from which a dose-response relation could be derived. In Paper I the measured effect was growth inhibition (GI) of tumors and in Paper II the effect was reduction in kidney function. Both parameters were measured at a certain time after α-RIT and the respective dose-response curves are presented in Figure 1. If the kidneys were assumed to be the primary dose-limiting organ in an experimental treatment with ^{211}At-MX35-F(ab')$_2$ and the maximal acceptable reduction in renal function was 50% of the function before treatment, the dose-response curve can be used to estimate the MTD for the kidneys. From the plot (Fig. 1, red squares) it can be seen that the renal function is reduced to a 50%-level at an absorbed dose to the kidneys of approximately 8 Gy, the MTD. According to the dose estimations in Paper II it was found that the dose to the kidney per unit administered activity of ^{211}At was 3.89 Gy per MBq. The MTD for the kidneys of 8 Gy thus corresponds to a MTA of approximately 2 MBq. In Paper I, the dose to the tumors per unit activity was found to be 4.09 Gy per MBq. If the experimental treatment were carried out at the MTA (for the kidneys) of 2 MBq, this would correspond to a mean absorbed to the tumors of approximately 8.4 Gy. As seen in the dose-response curve for the tumors (Fig 1, blue circles), the estimated effect on the tumors would correspond to a GI-value below 0.01. The tumor response to a fixed level of normal-tissue damage is often referred to as the 'therapeutic index'[63]. The relationship between the dose-response curves for the tumor and the critical normal organ at risk can be referred to as the 'therapeutic window' and it is this relation that governs if a therapy will be possible.

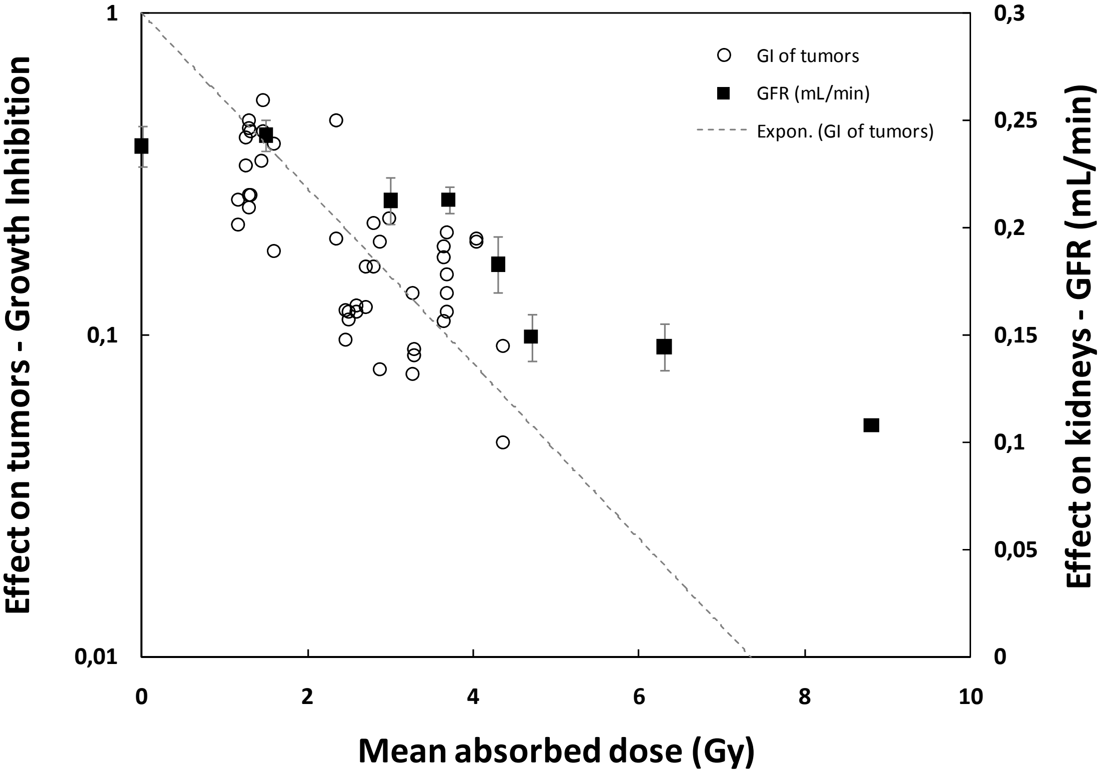

FIGURE 1. Example of a dose-response plot comparing the effects on tumors (growth inhibition) and kidneys (glomerular filtration rate) after α-RIT with i.v. injection of ^{211}At-MX35-F(ab')$_2$ in nude mice.

3. RBE OF α-RIT ON TUMOR GROWTH IN VIVO – Paper I

This study was carried out to evaluate the relative biological effectiveness (RBE) of ^{211}At for tumor growth after α-RIT in nude mice. Our endpoint was growth inhibition of subcutaneous xenografts and the reference was external irradiation with ^{60}Co. The α-RIT was done by intravenous injections of ^{211}At-MX35-F(ab')$_2$ antibodies at different levels of radioactivity (0.33, 0.65 and 0.90 MBq). The mean absorbed dose to tumors was calculated from a biodistribution study of tumor uptake of ^{211}At at different times after injection. External irradiation of the tumors was carried out as whole body irradiation of the whole mouse. The tumor growth was monitored by measuring the tumor volume at different times after α-RIT. The normalized tumor volume (NTV) was calculated by dividing each measured tumor volume with its corresponding initial volume. The growth inhibition (GI) was defined by dividing the NTV-values of the treated animals by those obtained from untreated tumors on control animals. To compare the biological effect of the two radiation qualities, the mean value of GI (from day 8 to day 23) was plotted for each tumor as a function of its corresponding absorbed dose. From exponential fits of these curves, doses required for a GI of 0.37 (D_{37}) were derived and the RBE of ^{211}At was calculated.

3.1 Definition of RBE

The RBE is defined as the ratio of the absorbed doses of a reference radiation, $D_r(x)$, (e.g. X-rays from ^{60}Co) and a test radiation, $D_t(x)$, (e.g. α-particles) that produces the same biological effect, x:

$$RBE(x) = \frac{\mathrm{D_r}(x)}{\mathrm{D_t}(x)}$$

Historically, the biological effects of α-particles have been studied in vitro by comparing with the effects of low-LET-radiation and the estimations of RBE have typically used the endpoint cell survival. A certain cell type is exposed to the two radiation qualities at different levels of absorbed dose and the cell survival after irradiation is plotted against absorbed dose. The doses required for a certain level of survival (e.g. a cell surviving fraction of 0.37) are estimated from the plot and used to calculate the RBE. The principle can be exemplified using a figure from a publication by Hall *et al.* [64] where cell survival after irradiation with high-LET α-particles (90 keV/μm) and X-rays (210 kV) was studied. Figure 2 shows their plot (reproduced with permission) and from the grey arrows (modification of the original figure), the doses required for a surviving fraction of 0.037 can be estimated to be ~950 rad (9.5 Gy) for X-rays and ~200 rad (2 Gy) for the α-particles. Thus, with x-rays as the reference, the RBE for the α-particle radiation using this endpoint would be ~4.8.

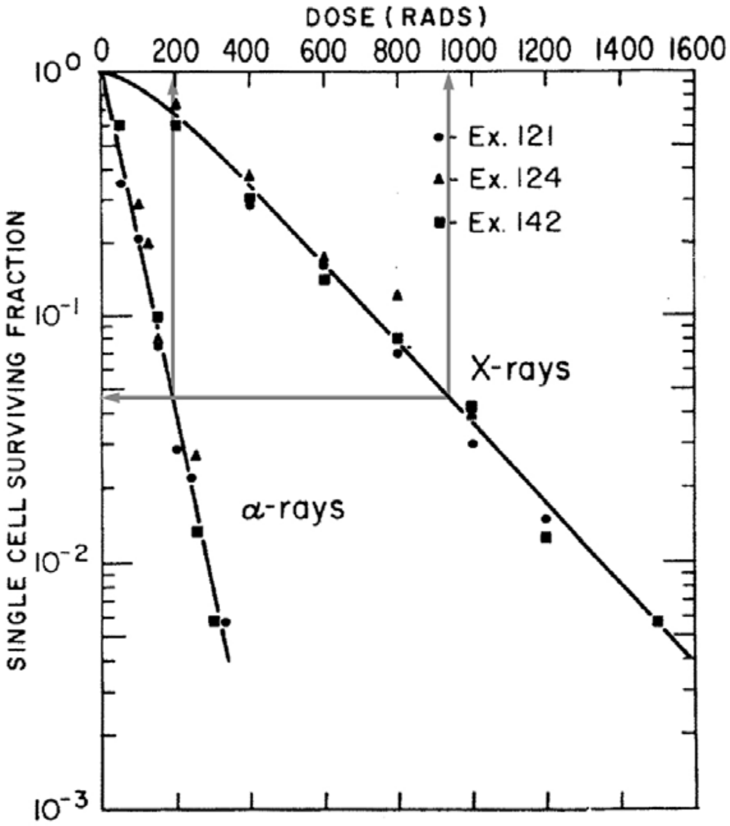

FIGURE 2. Example of RBE-estimation. 'Survival curves for asynchronous Chinese hamster cells exposed to 210-kV X-rays or alpha particles'. Modified from the original publication by Hall et al. in Radiation Research 52, 88-98 (1972). Reproduced with permission.

3.2 *in vivo*-RBE for α-RIT with ^{211}At on tumors

With ^{60}Co as reference, the *in vivo*-RBE of α-RIT with ^{211}At for growth inhibition of tumors was estimated to be 4.8 ± 0.7. The RBE was derived from the respective tumor dose required for a GI of 0.37 according to the plot in Figure 3.

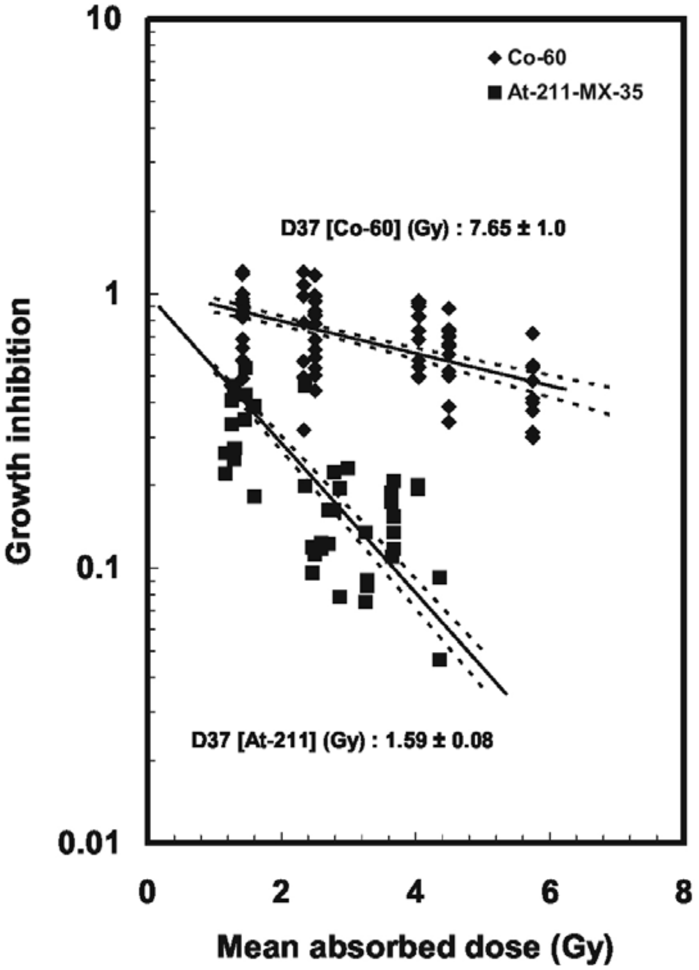

FIGURE 3. Growth inhibition for the two radiation qualities. The mean value (from day 8 to day 23) of GI for each tumor as a function of its corresponding mean absorbed dose. The unbroken lines represent the mono-exponential fits from which the absorbed doses required for a GI corresponding to 0.37 (D_{37}) were derived. For ^{211}At-irradiation the extrapolation number was forced to 1.0, while for ^{60}Co the extrapolation number was 1.04. Dashed lines indicate 67% confidence limits for the regression fit.

3.3 Factors influencing the estimation of RBE

The relative biological effectiveness (RBE) is one of the parameters by which α-emitters can be evaluated for use in RIT. In a strict radiobiological sense, the derivation of a RBE is only possible when there is exact knowledge and control on the measured biological effect as well as on the absorbed dose to the target causing the effect. In this perspective, any attempt to derive a RBE from an *in vivo* situation would be impossible, given the difficulties to achieve this knowledge. Already in the *in vitro* situation, estimations of RBE have inherent limitations that make comparisons difficult. Many of these difficulties are related to the higher variations in biological response of the low-LET-reference radiation than for high-LET radiation. This is reflected in the shapes of the dose-response curves; for high-LET the response is typically monoexponential, while for low-LET the shape changes (shoulder and bending) due to different factors like dose rate, dose level, oxygenic status and radiosensitivity of the cells. For low-LET, there is strong variation with dose rate on the slope of the dose-response curve. The probability for cellular repair is higher at low dose rates than at high dose rates. For high-LET, little variation is seen in the dose-response due to differences in dose rate [63]. With this as example, a high dose rate of the reference low-LET-radiation would give a lower RBE than if the dose rate was low and vice versa. This same is true for the factor of absolute dose level. At a low dose the probability of repair is relatively higher for low-LET and this corresponds to a higher RBE. As for radiosensitivity, the variations are markedly higher for low-LET than for high-LET [63]. For low-LET radiation, irradiated cells are typically more sensitive when oxygenated than hypoxic. The oxygen enhancement ratio (OER), estimating the oxygen effect, for low-LET is around 2-3 while for high-LET is typically 1. More generally, the RBE is varying with LET [65] so that the RBE increases up to a maximum around 100 keV/μm (which corresponds well to the LET of ^{211}At). It is believed that this maximum in RBE seen at a LET around 100 keV per μm, is related to the spatial distribution of ionizing events co-matching with the diameter of the DNA-helix (2 nm), making the probability of double-strand breaks (DSB) highest at this LET. Levels of LET higher than this become less effective per unit of absorbed dose, despite the higher deposited energy, and therefore the RBE again decreases.

The RBE can also depend on the cell cycle position of the irradiated cells, as reported early Hall *et al.* [64] and also recently by Claesson *et al.* [66]. Because of the short path length, the spatial distribution of the high-LET α-particles, in relation to the cells and their nuclei, will have a strong impact on the distribution of absorbed dose and this will affect the cellular dose-response. This effect has been described and discussed early by Fisher *et al.* and Humm *et al.* [67, 68], showing how the survival curve will depend on whether the α-decays occur in a surrounding medium only, or on the cellular membrane. The importance of non-uniform distribution have also been described by e.g. Howell and Neti [69, 70] and Kvinnsland *et al.* [71, 72]. Yet another factor will be the distribution of cellular size and shape. On the cellular level, the absorbed energy from α-particles to the nucleus of one individual cell can only be described in terms of probability, with a wide range of possible absorbed doses that needs to be estimated and modeled by microdosimetric approaches [59-61]. Thus, for α-particles the dose-response relationship will be impacted by microdosimetric effects from differences in source-to-target geometry [55] and thereby influence the RBE.

The biological effects on tumor growth following α-RIT observed in Paper I do not necessarily reflect absorbed dose to, and DNA-damages of, the tumor cells nuclei. Other effects, like bystander effects or radiation effects on vascular compartments, could also influence the growth inhibition. An RBE derived *in vivo* will be dependent on such effects, since they could be different for the two radiation qualities. Another important factor is the distribution of absorbed dose in the tumors. While the reference low-LET external ^{60}Co-irradiation had a very uniform dose distribution, this was not the case for the α-RIT. Despite all the factors mentioned and the limitations of deriving a RBE for α-particles from an *in vivo* endpoint like tumor growth, the estimated RBE of 4.8 ± 0.7 seems to be in agreement with values from a variety of other studies and endpoints. *Palm et al.* [73] estimated an *in vitro* RBE of 5.3 ± 0.7 for ^{211}At-albumin for cell survival of the same tumor cell line (OVCAR-3) as used in the *in vivo*-RBE of Paper I. The reference was ^{60}Co-irradiation in both cases. In two other *in vitro* studies of ^{211}At, both using fibroblasts, Kassis *et al.* [74] reported a RBE of 5.2 for survival using γ-photons from ^{137}Cs as reference and Claesson *et al.* [75] reported RBEs for DSB-induction of 2.1 and 3.1, with ^{60}Co and 70 kV x-rays as reference, respectively. In a recent study of ^{211}At from Claesson *et al.*[66], using DSB-induction and cell survival on fibroblasts, it was shown that the response was cell cycle dependent. This was observed for both low- and high-LET and corresponded to a variation in RBE from 1.8 to 8.6. In another *in vitro*-study, Akabani et al. [76] reported RBEs of 8.6–9.9 using cytotoxicity of ^{211}At-labeled trastuzumab on three different breast cancer cell lines. As for α-emitters other than ^{211}At, with the radionuclide labeled to monoclonal antibodies, RBE-values of 2-5 have been reported for ^{213}Bi [77] and 1.2-3.4 for ^{227}Th [78, 79] for different endpoints.

When it comes to estimation of RBE for α-particles for *in vivo*-endpoints, the information is limited. Harrison and Royle [80] compared the reduction in testes mass and in sperm numbers in mice after injection of ^{211}At, or exposed to X-rays (250 kV), and found a RBE of about 4. Howell *et al.* [81] also used a mouse testes model to study the RBE of ^{212}Pb in equilibrium with its α-emitting daughter nuclides (^{212}Bi and ^{212}Po). The RBE was 4.7 with 120 kV X-rays as reference. In this case, the α-irradiation was a mixed radiation field of photons, β-particles and α-particles. In another study, Howell *et al*. [82] estimated an RBE of 7.4 for the low-energy (3.2 MeV) α-particles of ^{148}Ga and 5.4 for the α-emitter ^{223}Ra (in equilibrium with its daughters). Only a few reports exist where estimations of RBE have been carried *in vivo* out in a α-RIT-setting. Using a similar endpoint as in Paper I, Dahle *et al.* [83] used tumor growth delay as an endpoint to estimate the RBE of a ^{227}Th-labeled antibody. With X-rays as the reference the RBE was between 2.7 and 7.2. With bone marrow toxicity as the endpoint, Elgqvist *et al.* [34] reported RBEs for ^{211}At-labeled antibodies of 3.4 and 5.0 using ^{99m}Tc-labeled antibodies and ^{60}Co as reference, respectively. Behr *et al.* [84] have reported a RBE of 1 for bone marrow toxicity using Fab' fragments radiolabeled with ^{213}Bi as compared to the β-emitter ^{90}Y. As an interesting comparison to the *in vivo*-RBE in Paper I of this thesis, the study by Behr also included estimation of RBE for tumor growth. The RBE found for antitumor effectiveness of ^{213}Bi-Fab' compared to ^{90}Y-Fab' was approximately 2-3. It is also interesting to note that, derived in the same experimental setting, the difference in RBE for bone marrow toxicity and antitumor effectiveness suggested an extra gain in the therapeutic window for the α-emitter. So far, this has not been shown in the setting of α-RIT using ^{211}At in our group [34, 85].

3.4 Summary of Paper I

With ^{60}Co as reference, the *in vivo*-RBE of α-particles on tumors was estimated to 4.8 ± 0.7, using tumor growth inhibition after α-RIT with ^{211}At-MX35-F(ab')$_2$ as the endpoint. Although estimations of RBE are afflicted with limitations, especially when derived *in vivo*, the RBE found is in good agreement with the range of values typically found for α-particles, 3-7 [53]. An RBE of 5 on tumors gives further support for the development of α-RIT, but once more precise knowledge can be obtained, both on the true absorbed dose levels to the tumor cells and on their cell survival, the values of RBE will have to be redefined. As indicated by one study [84], it would be advantageously supportive for α-RIT if RBE for tumor growth inhibition was found to be higher than for bone marrow toxicity.

4. RENAL FUNCTION AFTER α-RIT – Paper II

The kidneys are considered to be one of the tissues at risk in internal radiotherapy and also a late-responding tissue. In humans, renal damages can be manifested several years after radiation. The main reason for this is the slow turn-over rate of the renal cells[86] and the fact that radiation-induced cell death mainly occurs as cells attempt to divide. At a clinical follow-up of a patient treated with ^{90}Y-DOTATOC, Cybulla *et al.* found progressive renal failure 15 months after the last treatment [87]. Several studies on the effects of radiation on kidneys from internal irradiation have recently been presented within the field of peptide receptor radionuclide therapy. Valkema *et al*. reported that several patients showed a decline in creatinine clearance of more than 40% per year following peptide receptor radiation therapy with ^{90}Y-DOTATOC [88], with cumulative mean absorbed renal doses of approximately 27 Gy. In a study on the dose distribution in human kidneys, Konijnenberg *et al.* [89] used data from autoradiography to generate dose–volume histograms. They concluded that for high-energy β-emitters (e.g. ^{90}Y), the dosimetry could be based on the assumption of uniform activity distribution in the whole kidney, while for low-energy β-emitters (e.g. ^{177}Lu) and Auger-emitters (e.g.^{111}In) the dose distribution will be highly dependent on the distribution of activity within the kidney's substructures. Future improvements in dosimetry for the kidneys require multiregional model approaches, as described in MIRD Pamphlets 19 and 20 [90, 91].

The kidney is a highly complex organ both morphologically and functionally, and because of its complexity, special concerns are raised when the radionuclide is a α-emitter. The bioconjugates used in internal RT have a wide range of molecular weights, from below 10 kDa for peptides and engineered antibody molecules up to the 150 kDa for an IgG antibody. The pathways through the kidney of any molecule will depend on molecular size, but also shape and electrical charge. Depending on how the bioconjugate (and possibly released radionuclide) is distributed over time in the kidney and because of the short path length of α-particles in tissue, the variations in absorbed dose can be very high for different renal compartments. In this context, it is therefore relevant to recapitulate some of the basic features and functions of the human kidney.

4.1 The kidney and basic renal function

The main functional purpose of the kidneys is the homeostasis by which a stable internal environment for all cells in the body is maintained. This is achieved by a constantly ongoing process where the whole plasma volume, passing through the kidneys, is filtered and reabsorbed 75 to 80 times in a day. Important roles of this process are the regulatory functions (e.g. body water and salt balance) and clearing the blood plasma from metabolic rest products (e.g. creatinine and urea). The pathways through the kidney can be briefly exemplified with respect to three different molecules relevant to the studies of this thesis, namely ^{51}Cr-EDTA (Paper II), ^{211}At-MX35-F(ab')$_2$ (Paper I, II and III) and ^{211}At-Herceptin-IgG (Paper III), and compared with renal handling of the human serum albumin. In the passage of the kidneys, the size of a molecule is usually referred to in terms of the Stokes-Einstein radius (SE-radius) in nanometer. ^{51}Cr-EDTA is a small molecule used for estimation of renal function and has a molecular weight of 340 Da and a SE-radius of 0.48 nm [92]. The weight of a F(ab')$_2$ antibody fragment is 95 kDa (SE-radius ~3.8-4.4 nm)[93, 94] and a IgG is ~150 kDa (SE-radius 5.4 nm) [95]. Human serum albumin finally has a weight of 67 kDa (SE-radius 3.5 nm) [95].

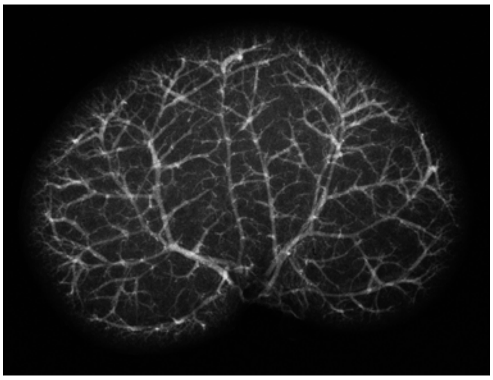

FIGURE 4. Angiography of a rat kidney visualizing the vascular branches. The image was produced and kindly provided by Ragnar Hultborn.

The functional unit in the kidney is the nephron, which can be described as having different functional parts put together as a long tube (Figure 5). A molecule in the blood will enter the kidney via the renal artery that is divided further into vascular branches (Figure 4) heading towards the renal cortex. Eventually these arteries end up as separate thin arterioles. Each afferent arteriole is split and folded into a net of capillaries called the glomerulus. The blood plasma is filtered over the glomerular capillary membrane across the glomerular barrier into Bowman's capsule, forming the primary urine. In a human approximately 180 L primary urine is produced in a day, corresponding to a glomerular filtration rate of 125 mL per minute. Of the 180 L primary urine produced, only 1.5 L is finally excreted as urine.

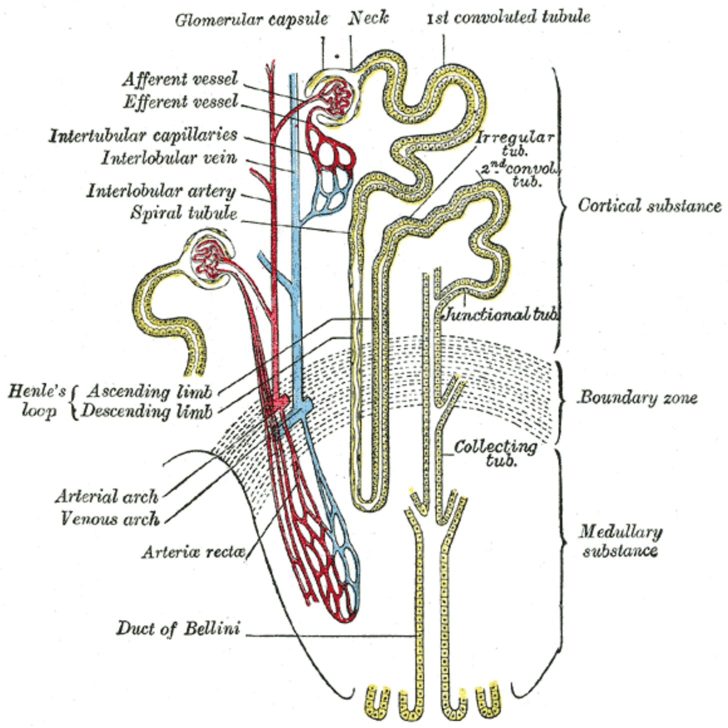

FIGURE 5. Some anatomical features of the kidneys. Reproduction of a lithograph plate from Gray's Anatomy. The image is in the public domain.

It is in the passage over the glomerular barrier that molecules will differ a lot, depending on their size, shape and charge. Small molecules (up to 1.5 nm) pass almost freely while larger molecules like proteins is largely restricted from passage. As for the molecules mentioned above, ^{51}Cr-EDTA will pass freely, while albumin and the IgG will be almost completely restricted. The sieving mechanism of the glomerular barrier can be described in terms of 'urine-to-plasma-concentration ratio' and as an example the approximate concentration of albumin in the primary urine is 0.1% of that in plasma, corresponding to a ratio (sieving coefficient) of 0.001. Despite its larger size, an IgG is estimated to have approximately the same sieving coefficient as albumin[95]. This is an effect of the charge selectivity of the glomerular barrier, restricting negatively charged molecules (e.g. albumin) more than neutral molecules of the same size. The molecular configuration can be even more important than the size and charge and molecules of elongated shape pass more readily to the urine [95]. The size and charge dependency on the transglomerular passage of molecules can be seen in Figure 6 (adopted with permission from a review by Haraldsson *et al*. [95]). The dependency of size, and also charge, on the sieving coefficient is strong for SE-radii from 2 nm up to 4.5 nm. As for a $F(ab')_2$ antibody fragment (considered neutral in charge), a SE-radius of 4-4.5 nm would correspond to a sieving coefficient of around 0.003–0.02, meaning that the concentration in the primary urine would be 0.3%–2% of that in plasma. The fraction of molecules not filtered through the glomeruli will return with the blood via the efferent arterioles.

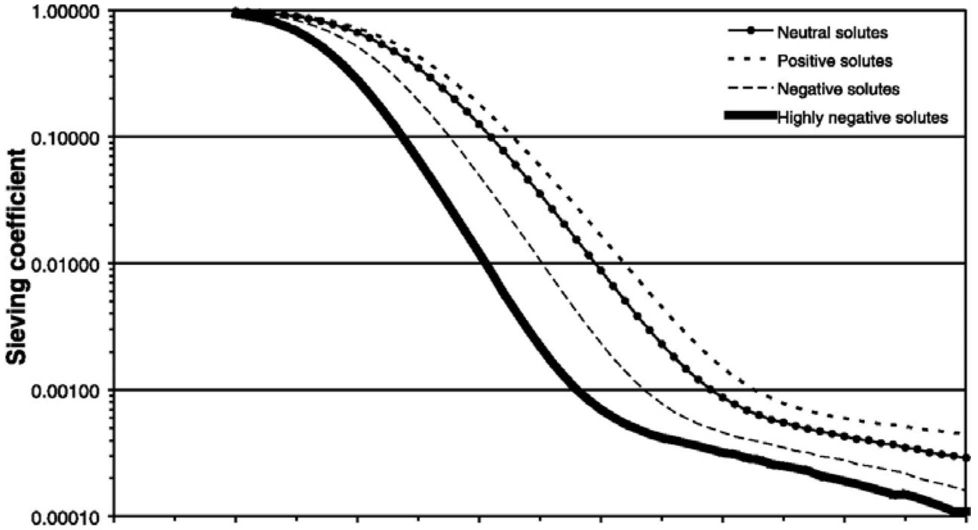

FIGURE 6. The fractional clearance or sieving coefficient of a solute plotted against its Stokes-Einstein radius. From the top, the curves represent slightly positive solutes, neutral solutes, negatively charged solutes, and highly negative solute charge similar to that of albumin. Adopted from a publication by Haraldsson et al. in Physiol Rev 88: 451-487, 2008. Used with permission.

From Bowman's capsule, the primary urine is lead into the tubular nephron, divided into the proximal tubule, the loop of Henle and the distal tubule. The distal tubules from 5 – 10 nephrons are connected in collecting tubules that are further connected via collecting ducts that eventually empty the urine from the kidney. Even though the regulatory mechanisms in the tubular system are complex and cannot be described here, some of the features are more relevant in the context of targeted radiotherapy, for instance the process of reabsorption of albumin in the proximal tubules. The fraction of albumin that passes the glomerular barrier will be taken up by the proximal tubular cells via the megalin-cubulin complex [96, 97]. A small increase in albumin concentration in the urine is an early sign of renal impairment. After lysozomal degradation of the albumin in the proximal tubules, its amino acids are released to the blood. The megalin-cubulin transporter is believed to be the mechanism behind the high uptake of radiolabeled peptides in proximal tubules [98], where the radiometals (e.g. ^{111}In and ^{177}Lu) are retained intracellularily leading to irradiation of the renal parenchyma (the functional cells).

In conclusion, the complex physiology of the kidney contributes to its complexity as a dose limiting organ in targeted radiotherapy. The effects from radiation in the kidneys will be governed both by characters of the targeting molecule (e.g. size) deciding the compartmental distribution, as well as of the radionuclides (e.g. path length of the emitted particles) deciding the subsequent distribution of absorbed dose.

4.2 Estimation of GFR

The glomerular filtration rate (GFR) is the rate (mL/min) at which the primary urine is produced when the plasma is filtered across the glomerular barrier. Measurement of GFR is generally accepted as the most important parameter to estimate the renal function and impairment. The golden standard method to estimate GFR is measurement of renal clearance of inulin after constant infusion and urine collection. In patients, this is a complex method that also introduces risk of infection from the bladder catheterization. If it can be assumed that a GFR-marker is not metabolized and is eliminated only through the kidneys via glomerular filtration (without tubular reabsorption or secretion), the total plasma clearance of the marker will equal the GFR. One such marker that has been clinically established in Scandinavia is ^{51}Cr-EDTA. The principle method of estimating GFR with ^{51}Cr-EDTA includes one intravenous injection of the marker followed by serial blood sampling to measure the decrease over time of the plasma concentration; the clearance of the marker from the plasma. With the assumptions above, the plasma clearance corresponds to the renal clearance and also the GFR. Generally, 2-4 blood samples are taken in the mono exponential phase to measure the plasma concentration and disappearance rate of the marker. The GFR is calculated by dividing the total injected amount of the tracer, Q, with the 'area under the curve', AUC, for the plasma concentration curve; so that $GFR = Q/AUC$. The AUC can be calculated by a mono exponential fit of the plasma curve using the slope, m; and the intercept, i; so that $AUC = i/m$.

In Paper II, the GFR was estimated from measurements of the plasma concentration at 3 time points after injection. Following a pilot study, these time points were chosen to represent the mono exponential phase of the plasma curve. Since GFR measurement in a mouse is experimentally difficult, the time points also had to be logistically possible in relation to the experimental design (e.g. number of animals per group). The typical time points used were approximately 10, 20 and 40-50 minutes after injection and as seen in Figure 7, this time interval matched the exponential phase very well.

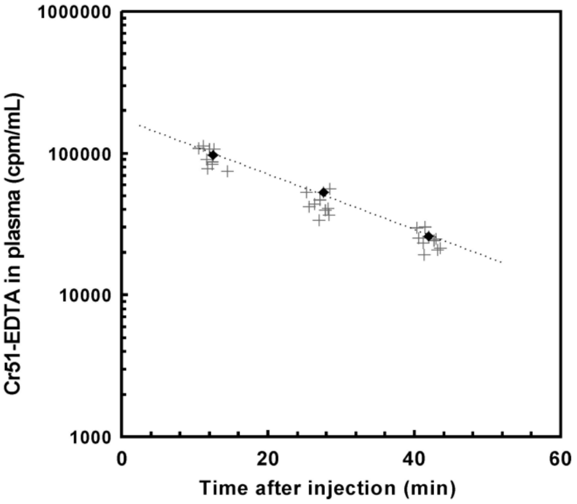

FIGURE 7. Example of a semi-log plot of the ^{51}Cr-EDTA plasma concentration versus time, used to estimate the GFR. The filled symbols (♦) represent data from a GFR measurement on one individual animal, and the corresponding regression line giving the slope and intercept is shown (dotted line). Individual GFR data from the other animals in the same study group on this occasion are also given in the plot (+).

Figure 8 is a plot from the pilot study which included later time points, up to 300 minutes after injection. As seen from this figure, the plasma concentrations for the later time points deviated from the exponential fit (10-50 minutes), and seemed to reach a lower plateau value of around 0.1%IA/g. This is likely to reflect other mechanisms than renal clearance of the plasma and one explanation could be uptake and accumulation of ^{51}Cr-EDTA in proteins. Included in Figure 8, is an exponential line between a theoretical initial plasma concentration (100%IA in a total of 0.675 g plasma in a mouse) and the first measured value at 12 minutes after injection. This visualizes how the true AUC is underestimated when the area (marked in grey) representing high plasma concentration during the early distribution phase is neglected. However, the blood sampling needed to assess the true AUC was not experimentally possible in our mouse study.

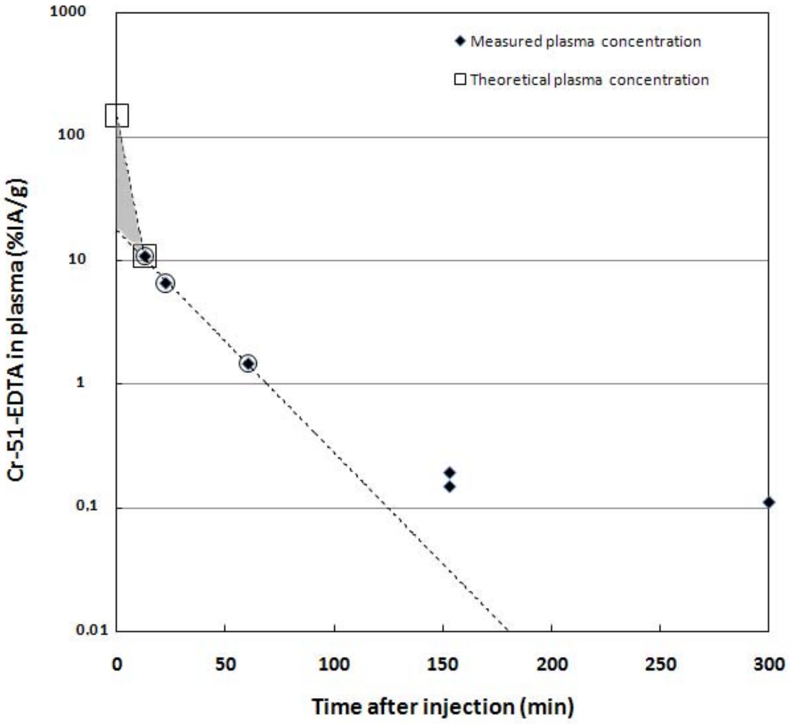

FIGURE 8. Plasma concentration of ^{51}Cr-EDTA as a function of time after injection.

In humans, estimates of GFR are usually normalized to a standard body surface area (mL x min^{-1} x [1.73m^2]$^{-1}$). In our mouse study we tried to analyze the data by normalizing the measured GFR of the individual animal to its body weight, but no obvious correlation was found (data not shown). For the irradiated animals there was however a clear relative reduction in the body weights. One year after treatment, the body weight of the untreated animals had generally increased from 20 g to 25 g. For the irradiated animals the weights generally remained stationary around the initial 20 g, except for the groups receiving the highest injected activities that showed a slight decrease in body weight.

4.3. Reductions in GFR after α-RIT

Following α-RIT with ^{211}At-MX35-F(ab')$_2$, a clear dose-response relation between GFR and mean absorbed dose to the kidneys could be observed. As can be estimated from the slopes of the plots in Figure 9, the reductions in GFR with increasing dose was progressive with time. The study was conducted both in tumor-bearing and non-tumor-bearing mice and when the GFR-reductions was compared at two different time intervals (8-30 and 31-67 weeks after α-RIT), the progressive pattern was observed for both groups. For the tumor-bearing animals, the dose required for a 50% reduction in GFR decreased from 16 ± 3.3 to 7.5 ± 2.4 Gy, as estimated from the early and late time interval, respectively. For the non-tumor-bearing animals the dose required decreased from 14 ± 4.1 to 11.3 ± 2.3 Gy. This underlines the importance of long-term studies when evaluating radiation effects on renal function.

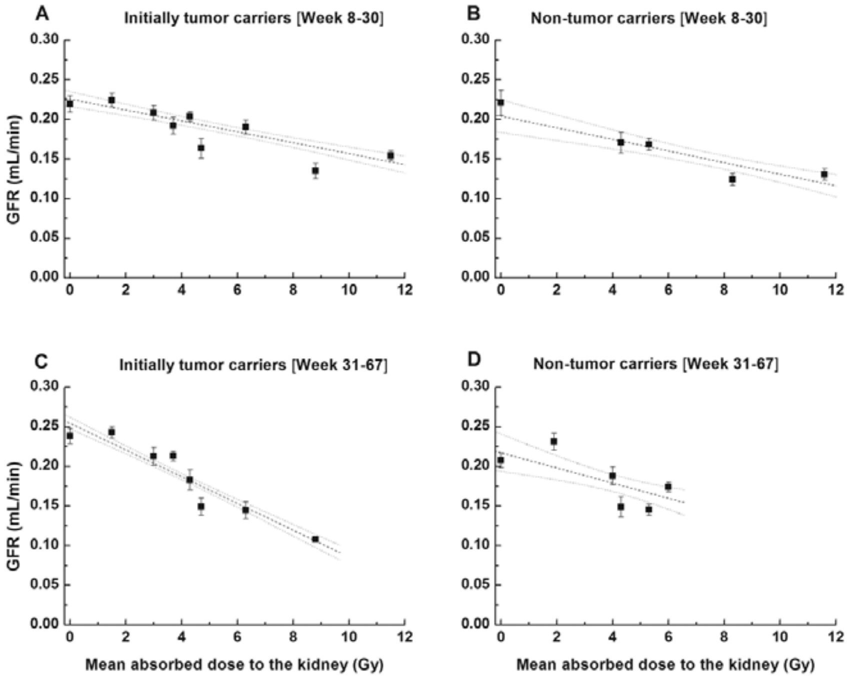

FIGURE 9. GFR estimates (means ± SEM) from each dose group plotted as a function of mean absorbed dose to the kidneys. Panels A and C present plots for the tumor-bearing animals at the time intervals 8–30 (n=190) and 31–67(n=120) weeks after the first administration of ^{211}*At, respectively. Panels B and D show the same time intervals for the non-tumor-bearing animals (n=40 and 80, respectively). Dashed lines represent linear regression fit, with 67% confidence intervals of the mean (dotted lines).*

The GFR is the sum of filtration rate in each functional nephron (single nephron GFR) and therefore the GFR could be used as a measure of the functional renal mass. In clinical practice it has been observed that a loss of nephrons can be invisible due to compensatory changes in the surviving nephrons [99]. For instance, it has been observed that a loss of half the functioning nephrons lead only to a decrease of 20-30% in GFR [100]. At the animal autopsy in our study, after the last GFR-measurement, the kidneys of the irradiated mice were observed to be markedly smaller than for the untreated mice. It would have been interesting to analyze a correlation between the GFR and the total kidney mass, but unfortunately the kidneys were not weighed at sacrifice. The mean GFR found in our study for all measurements (n=102) on all untreated (female) mice was 0.224 ± 0.062 mL/min (mean ± SD). In a study using mice of the same strain and the same GFR-marker (^{51}Cr-EDTA), the mean GFR found was 0.315 mL/min for females and 0.407 for males [101, 102]. Interestingly, the mean body weights in that study were 22.5 g and 27.7 g, respectively, meaning that if the GFR was normalized to body weight ($\text{mL} \cdot \text{min}^{-1} \cdot \text{g}^{-1}$), both sexes would have the same approximate value(14.0 versus 14.7 $\text{mL} \cdot \text{min}^{-1} \cdot \text{g}^{-1}$).

4.3. Serum creatinine

Since measurements of GFR using exogenous filtration markers are costly and time-consuming, other methods to assess renal function are commonly used in clinical praxis. The most common endogenous marker is determination of creatinine in the serum. Creatinine derives from metabolism in the muscles and is synthesized at stable day-to-day rate (approximately 20 mg/kg body weight in humans) in correlation with the muscle mass. Creatinine is almost completely filtered by the glomeruli and an increasing serum concentration is an indicator of a decreasing GFR and an impaired renal function. Estimations of GFR (eGFR) can be made using measured serum creatinine concentration and different empirical equations [103]. The serum concentration is dependent on several individual parameters like body weight, muscle mass, sex, age and nutritional intake. Even though these parameters are included in the eGFR-equations, they still contribute to the fact that serum creatinine is a very rough estimate on renal function. Generally, signs of renal impairment as detected from an increased creatinine concentration are not seen until the GFR is reduced to half of its normal value. Because of this, creatinine is a poor tool to detect early and moderate reductions in renal function.

The study in Paper II of this thesis included measurement of the serum creatinine at the time of sacrifice of the mice. The data suggested a dose-dependent increase in creatinine concentration with increasing mean absorbed dose to the kidneys. As seen in Figure 10, it was not until around a dose level of 10 Gy that the creatinine concentrations were elevated above the range (marked in grey) corresponding to the variations in mean for the untreated mice. It was concluded in that study that the maximum tolerable mean absorbed dose to the kidneys following α-RIT with ^{211}At-MX35-F(ab')$_2$, corresponding to a 50% decrease in GFR, was estimated to be approximately 10 Gy. These data seem to visualize the limitations of serum creatinine as a good marker for renal impairment, at least in mice.

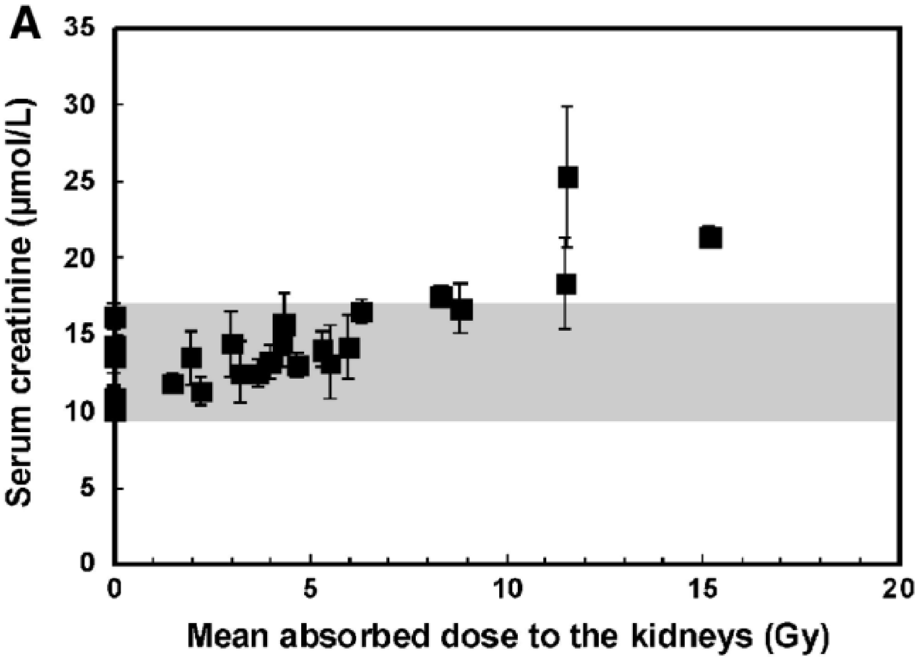

FIGURE 10. Levels of creatinine (means ± SEM, n=146) at the time of sacrifice as a function of mean absorbed dose to the kidney. The plot was created using all data, representing a time interval from the first α-RIT to sacrifice of 11 to 67 weeks.

4.4. Serum urea

An increase in the serum concentration of urea is also an indicator of renal impairment. Using antibodies labeled with the α-emitter ^{225}Ac, Jaggi *et al.* [104] found urea levels, starting at 20 weeks, that increased progressively with time after α-RIT in mice. For an estimated absorbed dose to the whole kidney of 27.6 Gy (39 Gy to the cortex) they found an urea concentration of 36 mmol/L. As can be seen in Figure 11, no clear dose-response could be seen for urea in Paper II. It should be noted that both for serum urea and creatinine, the measurements were conducted when the mice were sacrificed and that the data presented here is compilation of all data, representing a time interval from the first α–RIT to sacrifice of 11 to 67 weeks. A few individuals had values markedly elevated from the mean of the non-irradiated animals (8.3 ± 1.7, mean ± SD) but they are likely to be outlayers and they were separated from their respective group means by two standard deviations.

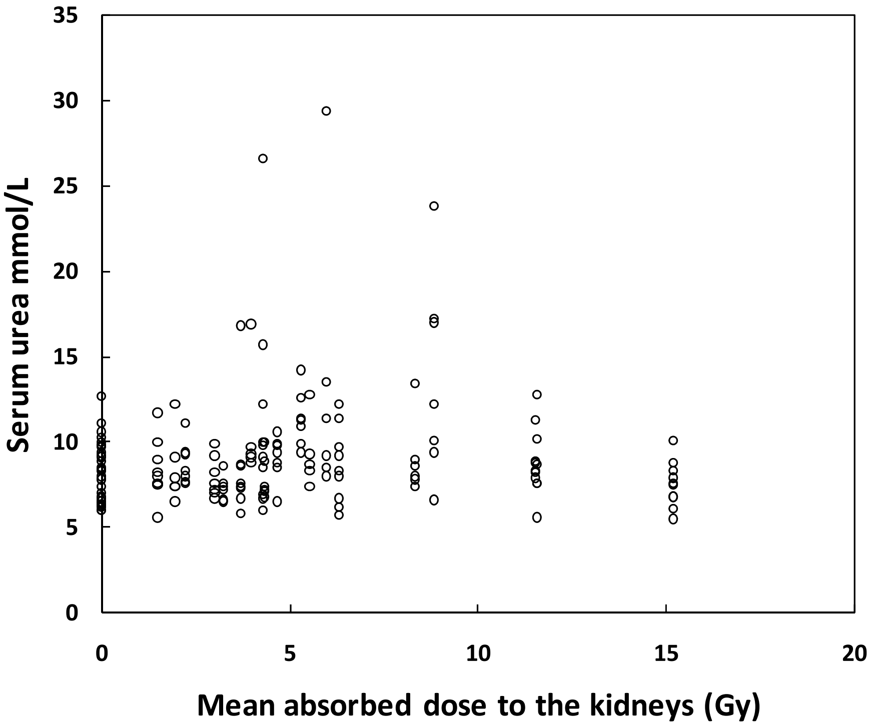

FIGURE 11. Levels of serum urea (n=145) at the time of sacrifice. The value of each individual animal was plotted as a function of mean absorbed dose to the kidney. The plot was created using all data, representing a time interval from the first α-RIT to sacrifice of 11 to 67 weeks.

4.5. Serum cystatin C

Serum cystatin C is a novel marker for kidney function and in contrast to creatinine, the serum concentration is independent of muscle mass, sex and age [103]. Thus, cystatin C is a more reliable parameter for renal disease. Cystatin C is plasma protein (13.4 kDa) that is synthesized at a constant rate by all nucleated cells and excreted into plasma. It is filtered by the glomeruli, reabsorbed and metabolized by the proximal tubules. Increasing serum levels of cystatin C is an indicator of reduction in GFR [103]. Analysis of cystatin C at the time of sacrifice was included in the study of Paper II and surprisingly, as can be seen in Figure 12, the serum levels decreased with increasing dose. We believed the explanation for this is thyroid dysfunction after α–RIT. It has been shown that cystatin C levels is affected by thyroid dysfunction and is therefore not a good marker of renal function in such cases [105].

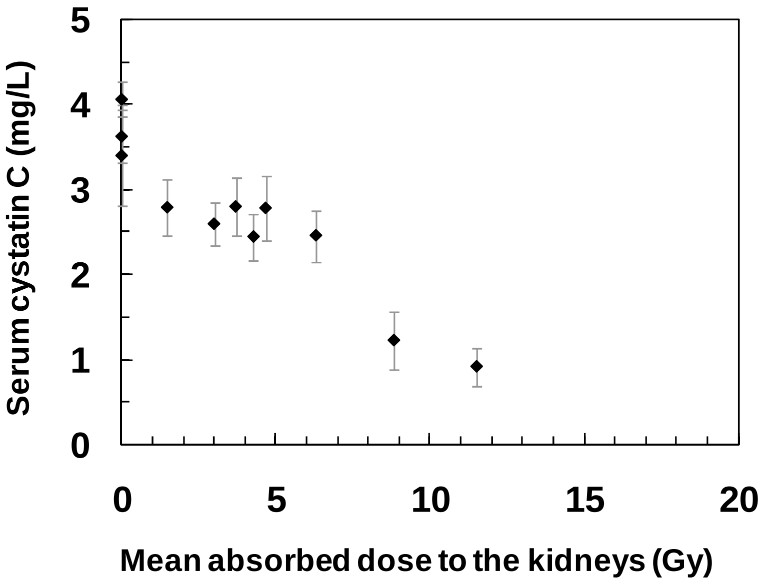

FIGURE 12. Levels of cystatin C (means ± SEM, n=31) in tumor-bearing animals at the time of sacrifice as a function of mean absorbed dose to the kidney. The plot was created using all data, representing a time interval from the first α-RIT to sacrifice of 11 to 67 weeks.

4.6. Histological findings

The histological changes of the kidneys after α-RIT were overall subdued. None of the glomeruli were sclerosed, no necrotic areas and no inflammatory infiltrates could be seen regardless of absorbed dose or time of sacrifice. The kidneys exposed to the highest level of absorbed dose (15.2 Gy) demonstrated discrete histological changes with some of the glomeruli reduced in size and appearing pre-sclerotic. Similar glomerular changes but at a lesser degree were found in the kidneys exposed to 8.8 Gy, regardless of the time frame. However, the animals that received 8.8 Gy and were followed for an extended time (sacrificed at 37 weeks), as compared to the animals sacrificed at week 20, did show focal areas of cortical tubular atrophy. Thus, the development of tubular atrophy is a process that requires time and, as judged from the material of Paper II, the histological changes require at least six months to develop.

4.7. Summary of Paper II

It was concluded that a mean absorbed dose to the kidneys of 10 Gy should be tolerable, following α-RIT with ^{211}At-MX35-F(ab')$_2$. This dose corresponded to a decrease in GFR (50%) that could be acceptable in patients being treated for cancer. Overall, the reductions in GFR were considered to be moderate in relation to the rather high levels of absorbed dose to the kidneys. Due to the overcapacity of the kidneys, clinical symptoms start to arise in humans when the renal function is reduced to 20%.

The largest reductions in GFR were seen at late times (up to 67 weeks) after α-RIT, which correspond to approximately half the life time of nude mice. Not knowing the RBE for the endpoint in question, it is difficult to have an opinion of the dose, 10 Gy, estimated as a tolerable dose. In external beam RT, the generally accepted tolerable doses are 23 and 28 Gy for 5% and 50% risk of renal failure within 5 years[106], respectively. The results of Paper III, where a marked retention of the ^{211}At-MX35-F(ab')$_2$ could be observed in the renal cortex, suggests that any tolerable dose for α-RIT should not be defined for the kidney as whole, but instead for its subcompartments. This would allow translation of the tolerable dose to other modalities of α-RIT using other bioconjugates than ^{211}At-MX35-F(ab')$_{2.}$

5. THE ALPHA CAMERA – Paper III

The α-camera system was developed to be an imaging tool to improve the predication and understanding of the radiation effects of α-particles in tissues. The benefits of using α-particle emitters in targeted therapy, i.e. a highly localized and very cytotoxic irradiation, also constitute the major difficulties when it comes to identifying the dose-response relations. Even though large-scale dosimetry in terms of the mean absorbed dose to a whole organ may be valid in some cases to predict (or relate to) a certain biological effect, a more detailed knowledge of the absorbed dose distribution will be needed in many cases. Basically, a small-scale dosimetry model will demand information on two parameters; (1) the spatial distribution of activity over time and (2) correlated spatial information on the functional morphology of the relevant cells in the tissues or organs. As presented in Paper III, the α-camera gives quantitative measures on the activity distribution of α-emitting radionuclide on near cellular level and can be complemented with the morphological information from other digital imaging techniques.

Many studies have shown how autoradiography can use in the development and dosimetry of targeted α-RT. Humm *et al.* [107] used data from autoradiography of ^{125}I-labeled antibodies in mice tumor models to show how such data could be used for dosimetry of ^{211}At, utilizing the autoradiographic grains from ^{125}I as the spatial locations for ^{211}At-decays. A similar approach was used for α-particle microdosimetry in a study by Akabani *et al. [108]*, where the activity distribution of ^{125}I-labeled antibodies in lung tissue was obtained by autoradiography and assumed to be representative of that ^{211}At and ^{213}Bi. Autoradiography with ^{211}At has been used to register the α-particle tracks. Brown *et al.* [109] used autoradiography (aqueous nuclear emulsion) to visualize and quantify the cellular distribution α-particle tracks from a ^{211}At-drug in an *in vivo* tumor model and Larsen and Bruland [110] performed microautoradiography to detect α-particle tracks in tumor slices after intratumoral injection of ^{211}At-labeled antibodies in mice. Hassfjell *et al.* [111] visualized nonuniform distributions in bone structures of the bone-seeking radiopharmaceutical ^{205}Bi-DOTMP by autoradiography of the hind legs and vertebral bodies in mice. In a recent publication [112], photographic emulsion was used to visualize the distribution of α-particle tracks from ^{227}Th-rituximab in the bone marrow and the femoral bone surfaces in mice.

5.1. Principle of the α-camera

The α-camera is a digital autoradiography imaging technology using optical registration of photons emitted from a scintillator dedicated to α-particles. The geometric set-up of the section sample during imaging is schematized in Figure 13. Cryosections of tissues (Fig 13; A) containing an α-emitting radionuclide were transferred onto the scintillator (Fig 13; B). The α-particles (Fig. 13, black solid arrows) emitted in the tissue hit the scintillator and generate scintillation photons (Fig. 13, blue dotted arrows) that traverse the cryosection, before being imaged optically with a charge-coupled device (CCD)-detector. By using a macro–photographical setup, the magnification scale of the images could be varied to approach the microscopic level using a macro-photography setup. The acquired images allowed for quantitative analysis; pixel intensities were used to estimate the activity distribution of the radionuclide within the imaged cryosections. The scintillator used was zinc sulfide which was known already in 1903 when Crookes could visualize the individual scintillations caused by α-particles using his Spinthariscope [113-115]. Typically, autoradiograms are acquired with the tissue sections in direct contact with the radiation-detecting medium, and therefore the picture scale for each technique is generally fixed. A major advantage of the α-camera is the possibility of optically varying the picture scale. The resolution of the imaging system is not primarily limited by the optical registration of the scintillation photons. Therefore, the picture scale can be varied by altering the focal distance, allowing imaging of multiple or large specimens with only minor decrease in spatial resolution. The α-camera is placed inside a dark box and the set-up of the system is seen in Figure 14.

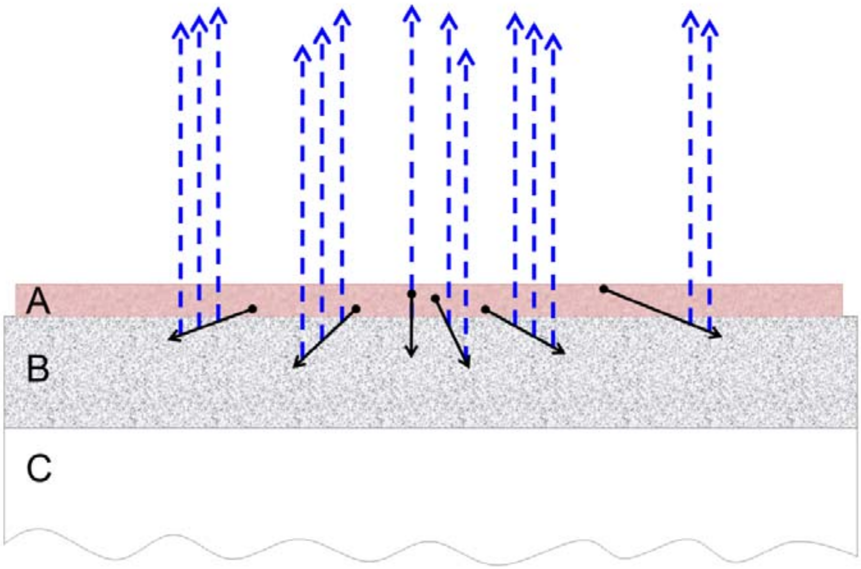

FIGURE 13. Schematized setup of sample configuration during α-camera imaging. Cryosections of tissues (A) are placed directly on the scintillating layer (B) that is coated on a clear polyester sheet (C). α-particles (black solid arrows) emitted in the tissue section hit the scintillator and generate scintillation photons (blue dotted arrows) which traverse the cryosection before being imaged.

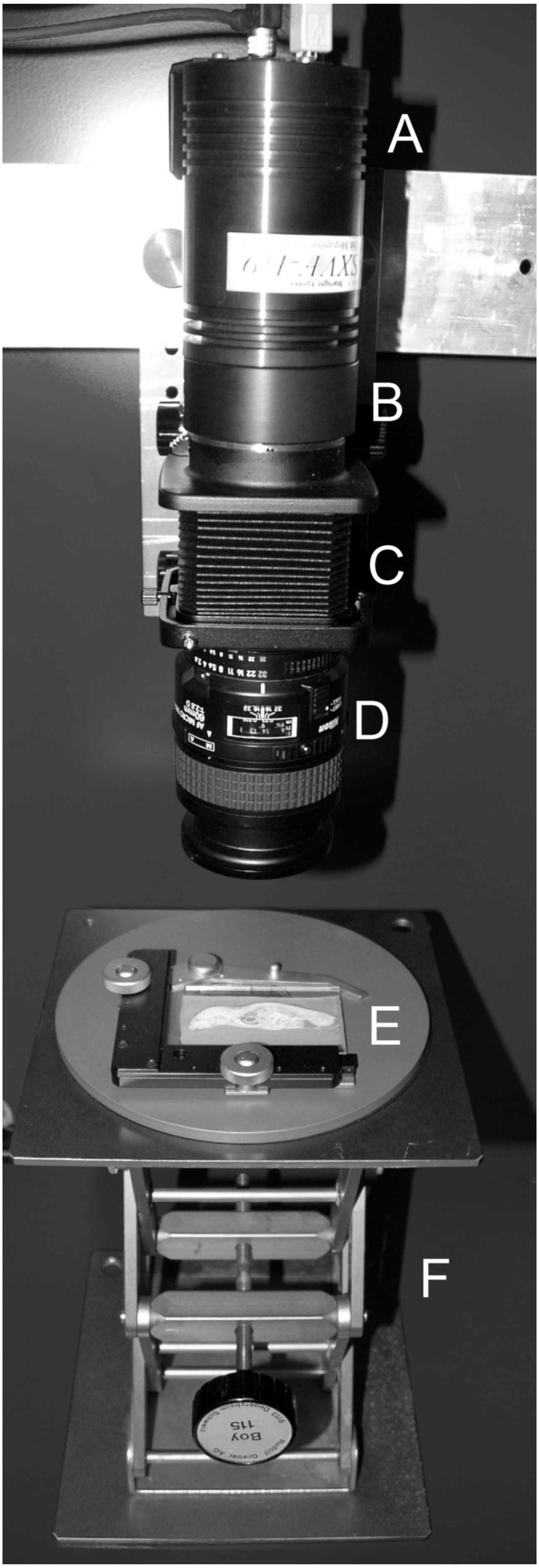

FIGURE 14. The setup of the α-camera, consisting of (A) CCD-detector; (B) lens adapter; (C) extension bellows; (D) optical lens; (E) glass slide holder; (F) adjustable stand.

5.2. Characteristics of the α-camera

The α-camera system appears to be a promising tool for small-scale dosimetry of α-particles. The system provides detailed information on the activity distribution in cryosections of tissues at almost a cellular level. The initial evaluation of the spatial resolution of the system, using radioactive line sources, corresponded to a FWHM (full width at half maximum) of 35 ± 11 μm. This was the mean (± SD) of 8 line profiles of which the best FWHM was 26 μm (presented in Figure 16A). From a qualitative point of view, comparing small morphological structures in the acquired α-images with superimposed histological images of the corresponding areas, the resolution seems to be even better; maybe less than 20 μm. The construction of line sources thin enough for estimation of FWHM was technically difficult. The line sources used were prepared from biological tissue and imaged in a geometrically set-up identical to the set-up for the tissue specimens. The FWHM found so far corresponds approximately to 2 to 3 times a typical cell diameter. Furthermore, the acquired α-images can be processed by digital imaging filtering, so that they more precisely represent the true spatial locations of the radionuclide decays. This can be done by deconvolution methods using the point spread function from an imaged point source.

An important characteristic of the α-camera is that the pixel intensity in the acquired images, following background corrections, is linear towards radioactivity in the imaged sample. The relation between pixel intensity and activity was possible to evaluate since the imaged specimens could be measured for activity after imaging, by use of a gammacounter. A linear relation was found for all the evaluated imaging situations, i.e. a radioactive solution directly applied to the scintillator (1), imaging of whole tissue sections (2) and imaging of certain areas of tissue (3). Figure 15A (Supplemental Fig. 2A of Paper III) shows the linearity from situation (1) from which the decreasing pixel intensity could be used to estimate decay of ^{211}At. The estimated half-life was 7.15 h, which is in good agreement with the actual half-life of 7.21 h. Figure 16B (Supplemental Fig. 3B of Paper III) presents the results from quantitative analysis of imaged kidney sections(2). The ROI (region of interest) data from the imaged kidneys (total pixel intensity per second in a whole-kidney ROI) was plotted versus measured ^{211}At activity in the same sample. As seen from figure XB, the linearity was very good over the whole range of activity (up to 3000 Bq in the imaged specimen), showing that the α-camera can be used for activity quantification. Even though the lowest detectable activity for ^{211}At has not been estimated, activities of 10–20 Bq in the cryosections at the time of imaging seem sufficient to demonstrate the radionuclide distribution and allow quantitative analysis.

The uniformity of the α-camera system was evaluated from imaging of plane sources of uniform activity. By comparing the relative standard deviation of the pixel intensity in different ROIs, placed over the image area, the estimated uniformity was below 2%. When analyzing the pixel-to-pixel intensity variations at different levels of pixel intensity, it was found the relative standard deviation of the mean of a ROI reached a lower level of approximately 2% when maximum intensity level (65k) of the 16-bit-images was approached (Figure 15B).

To estimate the reduction in signal due to the absorption of the scintillation photons during tissue passage (in direct relation to the thickness and optical density of the tissue section), the variations in light transmission of an imaged 16 μm whole-kidney section was analyzed. The effect of absorption at 450 nm (corresponding to the wave length of the scintillation photons) corresponded to a maximum intensity variation of approximately 10%. The effect of optical density variations can be corrected for by using a corresponding image of an adjacent section mounted on a glass slide.

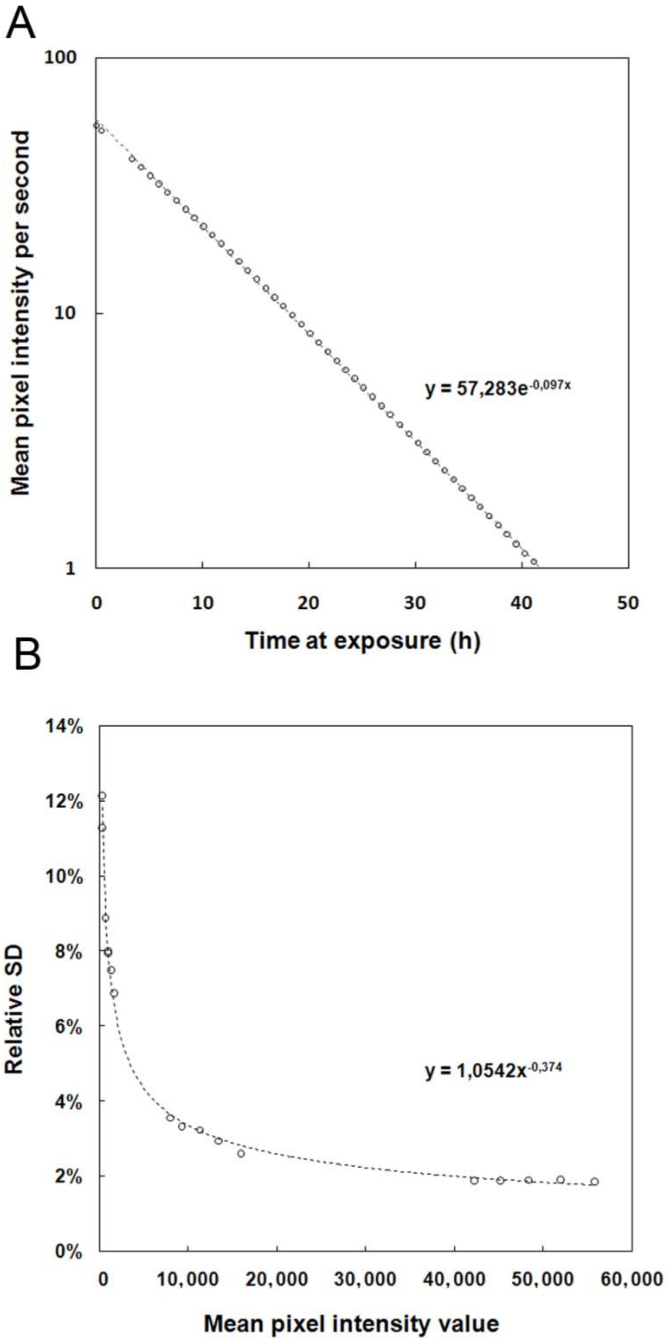

Figure 15. (A) The linearity of the α-camera system. The mean pixel intensity value per second plotted as a function of time for an ROI of a repeated-exposure series of a given decaying ^{211}At sample. The dashed line represents the exponential fit used to estimate the ^{211}At half-life. (B) Pixel-to-pixel intensity variation with pixel intensity. Relative standard deviation is plotted as a function of the mean pixel intensity value for an ROI of a repeated-exposure series of a given decaying ^{211}At plane source.

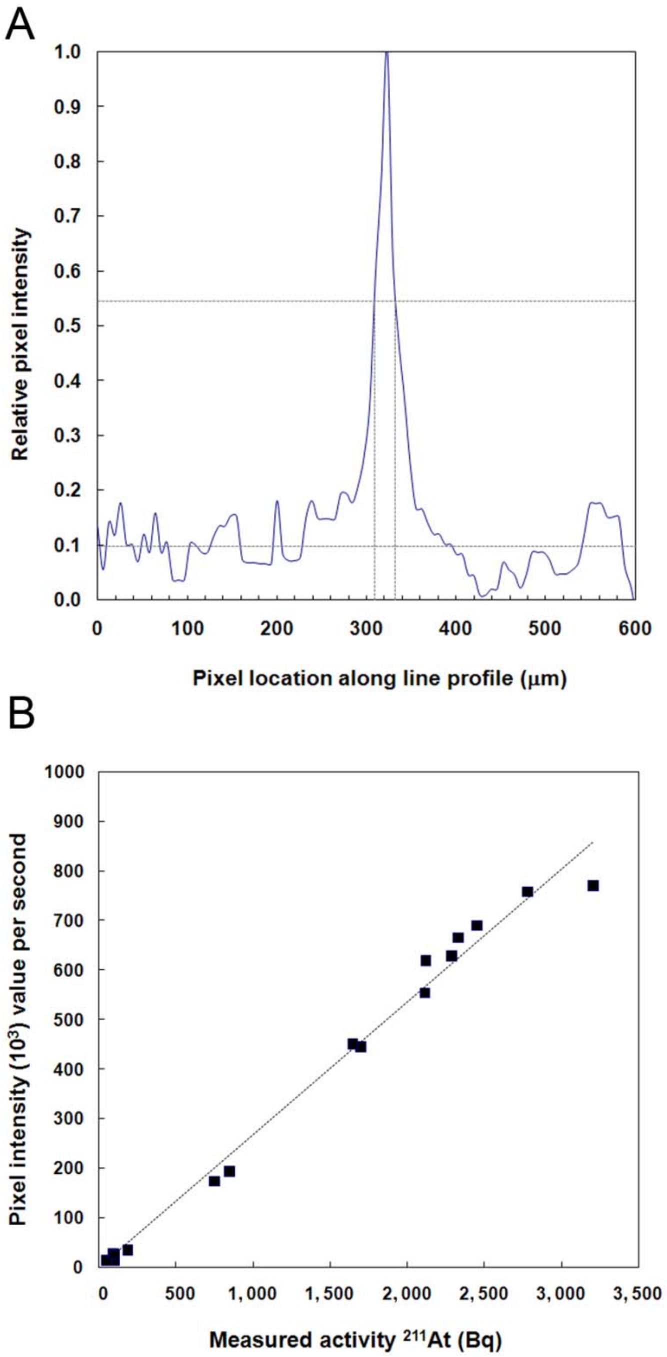

FIGURE 16. (A) Spatial resolution of the α-camera system. The pixel intensity values along the line profiles of an imaged line source are plotted as a function of pixel location. The dashed lines represent an estimated FWHM of 26 μm for one position along the line source. (B) Pixel intensity in α-camera images of kidney sections (quantified from ROIs) is plotted as a function of the measured ^{211}At activity in the corresponding sample.

5.3. Applications of the α-camera

Two major issues for the development of targeted radiotherapy were chosen to exemplify important applications of the α-camera: the penetration in tumors and the distribution in kidneys of the radioimmunoconjugates. For the tumors studies, we used a xenograft model of subcutaneous OVCAR-3 tumors, previously studied and described in Paper I. After intravenous administration of ^{211}At-MX35-F(ab')$_2$, the activity distribution in tumors was studied at different times after injection (10 min, 7 h and 21 h), by α-camera imaging of cryosections. The times were chosen to represent three different phases of intra-tumoral bioconjugate distribution: the vascular, capillary extravasation, and diffusion-with-binding phases [116]. The results are summarized in Figure 17 where it can be seen in the 10 minute images (1-3) that small areas were visualized (identified from H&E-staining as vascular compartments) with very high activity relative to the surrounding tissues. At 7 hours (4-7) there was markedly higher activity concentration in ring-shaped stromal compartments, surrounding clusters of tumor cells. A more uniform activity distribution was not seen until 21 hours after injection (8-9). Figure 18 present a quantitative analysis of the activity distribution from the images in Figure 17. ROIs were identified encompassing the whole tumor areas and the binned (256 bins) pixel intensities were normalized to the mean pixel intensity for the ROI and plotted versus the relative area (to total number of pixels in ROI) for each bin level. The histograms for 10 mpi and 6 hpi show a marked skewness resulting from the nonuniform activity distribution. In comparison, the histograms for 21 hpi seem to have a normal distribution corresponding to a more uniform activity distribution. Thus, the α-camera imaging revealed a highly nonuniform activity distribution of ^{211}At in the tumors after α-RIT and, because of the short path length of the α-particles, this will result in a very nonuniform dose distribution.

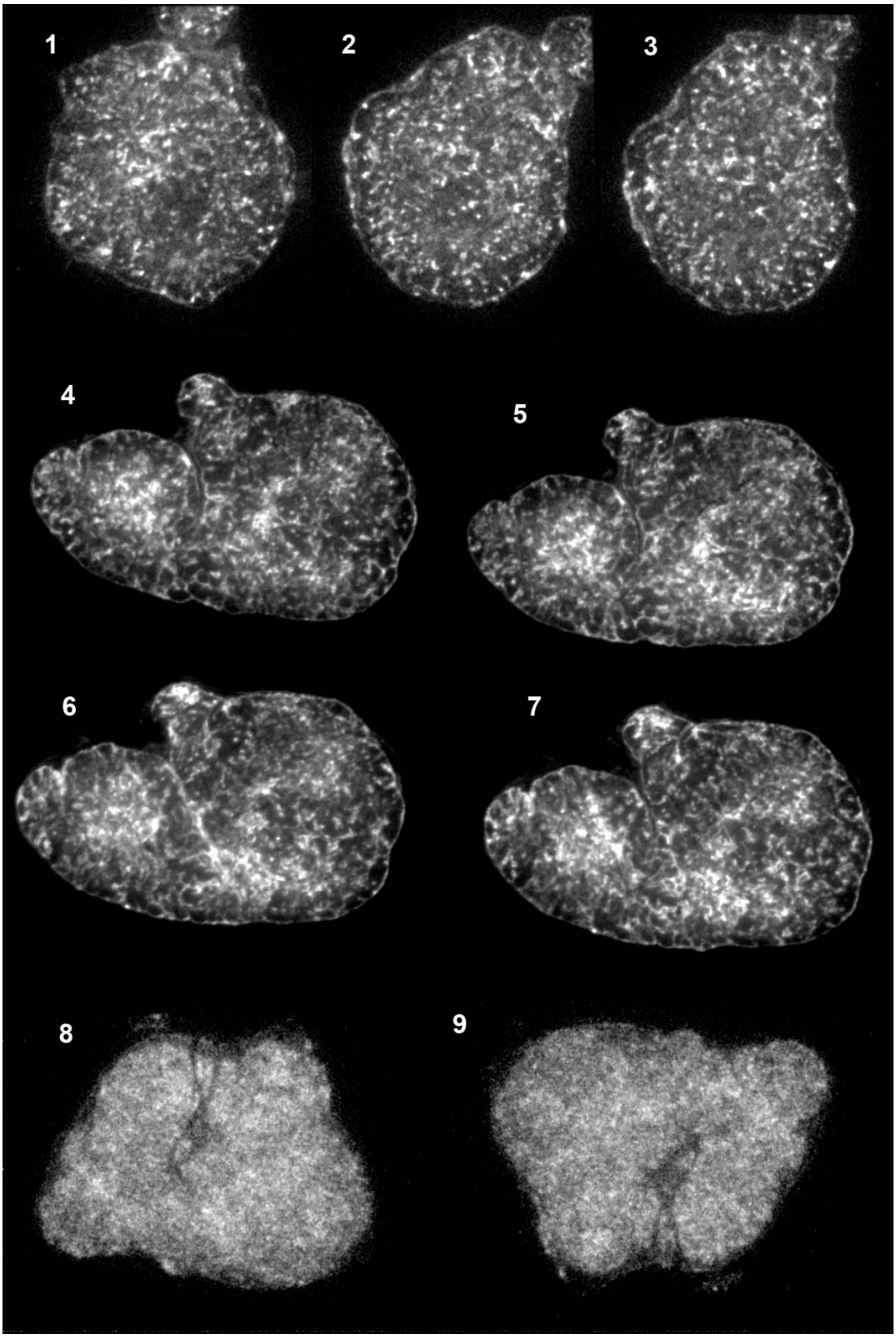

FIGURE 17. ***α-camera images of the activity distribution of ^{211}At-MX35-F(ab')$_2$ in s.c. OVCAR-3 tumors in nude mice at 10 minutes(1-3), 6 hours (4-7) and 21 hours (8-9) after intravenous injection. The imaged cryosections were 12-16 μm thick.***

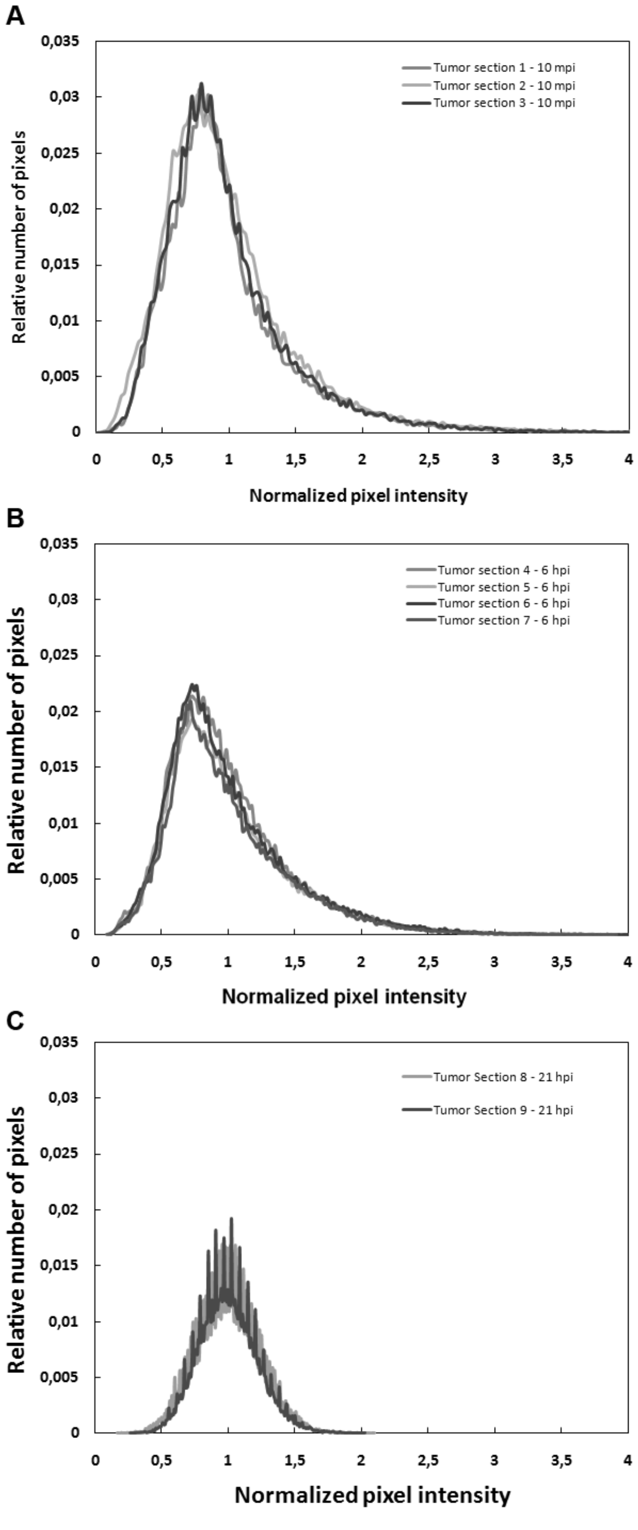

FIGURE 18. Histograms of the activity distribution in the α-camera tumor images in Figure 17, derived from ROIs encompassing the whole tumor areas. The binned (256 bins) pixel intensities were normalized to the mean pixel intensity for the ROI and plotted versus the relative area (to total number of pixels in ROI) for each bin level. A) 10 minutes, B) 6 hours and C) 21 hours after injection.

From α-camera imaging of the kidneys after α-RIT with ^{211}At it could be observed that the activity distribution in the different renal compartments varied with time after injection and was dependent on the antibody size. Figure 19 shows α-camera images of mice kidney cryosections. Image 1 in the figure shows the activity distribution of ^{211}At-IgG Trastuzumab 10 minutes after intravenous injection. Several kidney structures seem to be visualized in the image (Figure 19; 1), e.g. cortex with glomeruli, medulla with vascular branches stretching towards cortex and also the renal pelvis. The image representing ^{211}At-IgG at 2 hpi (Figure 19; 2), shows a similar distribution. In contrast, the activity distribution of ^{211}At-MX35-F(ab')$_2$ 2 hours after injection (Figure 19; 3) showed high relative activities in the renal cortex. A quantitative analysis, comparing ^{211}At-MX35-F(ab')$_2$ with ^{211}At-IgG Trastuzumab, showed that the relative activity distributions were similar after 20 minutes (Figure 20; A-B) but at 2 hours after injection there were clear differences (Figure 20; 4C-D). At 2 hours, the images disclosed a stronger retention of ^{211}At-MX35-F(ab')$_2$ in the renal cortex than for the IgG-antibody. This difference was further evaluated by imaging at a longer range of time points (10–480 minutes) after injection. For all time points studied the 'cortex-to-whole kidney'-ratio for the F(ab')$_2$-fragment were higher than for the IgG-antibody. At 2 hours after injection, the ratios (mean ± standard deviation) were 1.38 ±0.03 and 0.77 ±0.04 for ^{211}At-MX35-F(ab')$_2$ and ^{211}At-IgG, respectively.

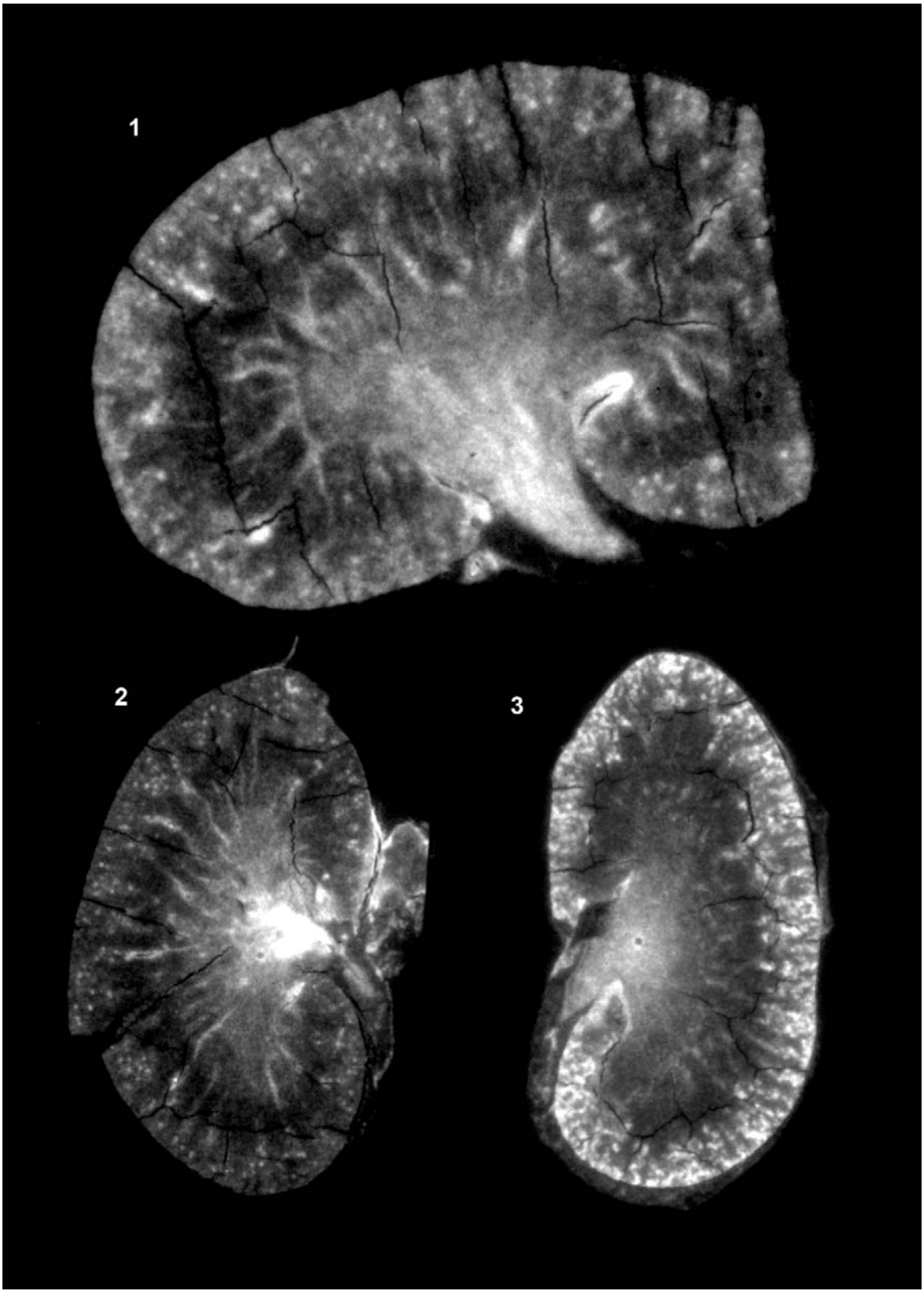

FIGURE 19 α-camera images of the activity distribution of ^{211}At-IgG Trastuzumab in mice kidney sections 10 minutes (1) and 2 hours (2) after intravenous injection. Panels (3) is ^{211}At-MX35-F(ab')$_2$ 2 hours p.i. The imaged cryosections were 12-16 μm thick.

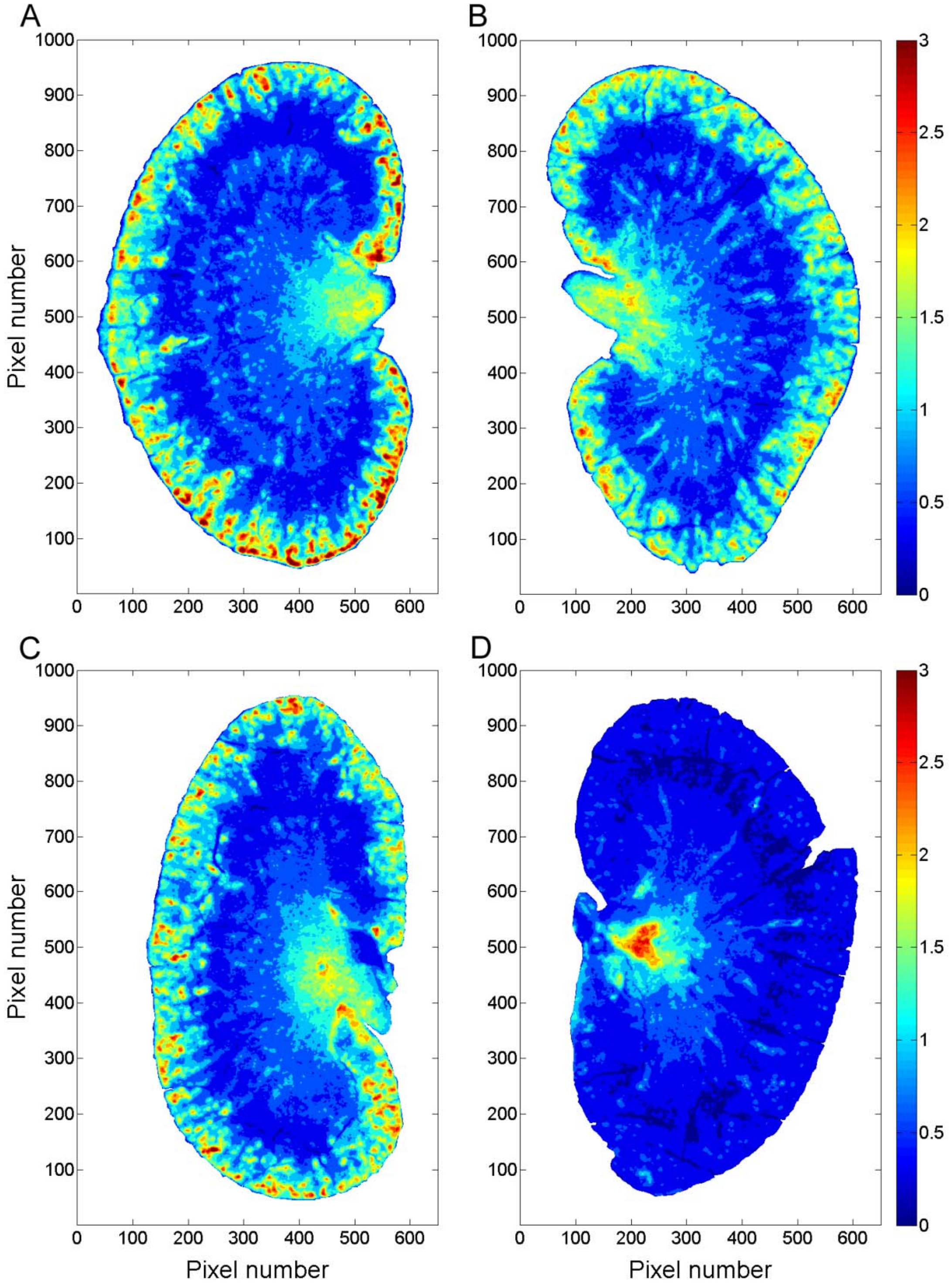

FIGURE 20. Activity distribution of ^{211}At-F(ab')$_2$ and ^{211}At-IgG Trastuzumab in kidneys 20 minutes (A, B) and 2 hours (C, D) after intravenous injection. The left panels (A, C) depict ^{211}At-MX35-F(ab')$_2$, while the right panels (B, D) display ^{211}At-IgG Trastuzumab. Each pixel intensity value was normalized to the mean pixel intensity of the whole kidney. The normalized data were divided into ten bins between 0 and 3.0, and each level was color-coded.

Alpha-camera imaging has also been conducted on a few different other normal tissues from mice following injection of either free ^{211}At or ^{211}At-labeled antibodies and some examples are shown in Figure 21. The top row is the liver (1), lungs (2) and the spleen (3) 4 hours after injection of ^{211}At-labeled 1F5, a murine anti-CD20 monoclonal antibody [117]. These images (1,2 and 3) are shown only to exemplify the α-camera imaging possibilities of different normal tissues. They were taken in collaboration with the research group of Oliver Press at the Fred Hutchinson Cancer Research Center in Seattle and belong to a series of α-RIT studies of lymphoma and leukemia. As illustrative and contrasting examples, the liver (1), representing a very uniform activity distribution and the spleen (2), representing a very nonuniform distribution, were used for the histograms presented in Figure 22.

Figure 21 (4 to 7) demonstrate the distribution of free ^{211}At in a nude mouse at 30 minutes after i.v.-injection. Alpha-imaging of whole body sections in the sagittal plane (4) visualized uptake in the organs that are known to accumulate free ^{211}At, e.g. the thyroid, stomach and the salivary glands. Sections at other sagittal planes visualized elevated uptakes also in the spleen and the lungs (data not shown). The thyroid (6) and the salivary glands (7) are blow-ups from the same exposure of the whole body-section (4), showing that even at the low picture required to image a whole mouse section, the resolution will be rather good. The bright areas along the spine in the whole body-section (4) were identified as cartilage. The last α-image (5) in Figure 21 is a cryosection of the stomach.

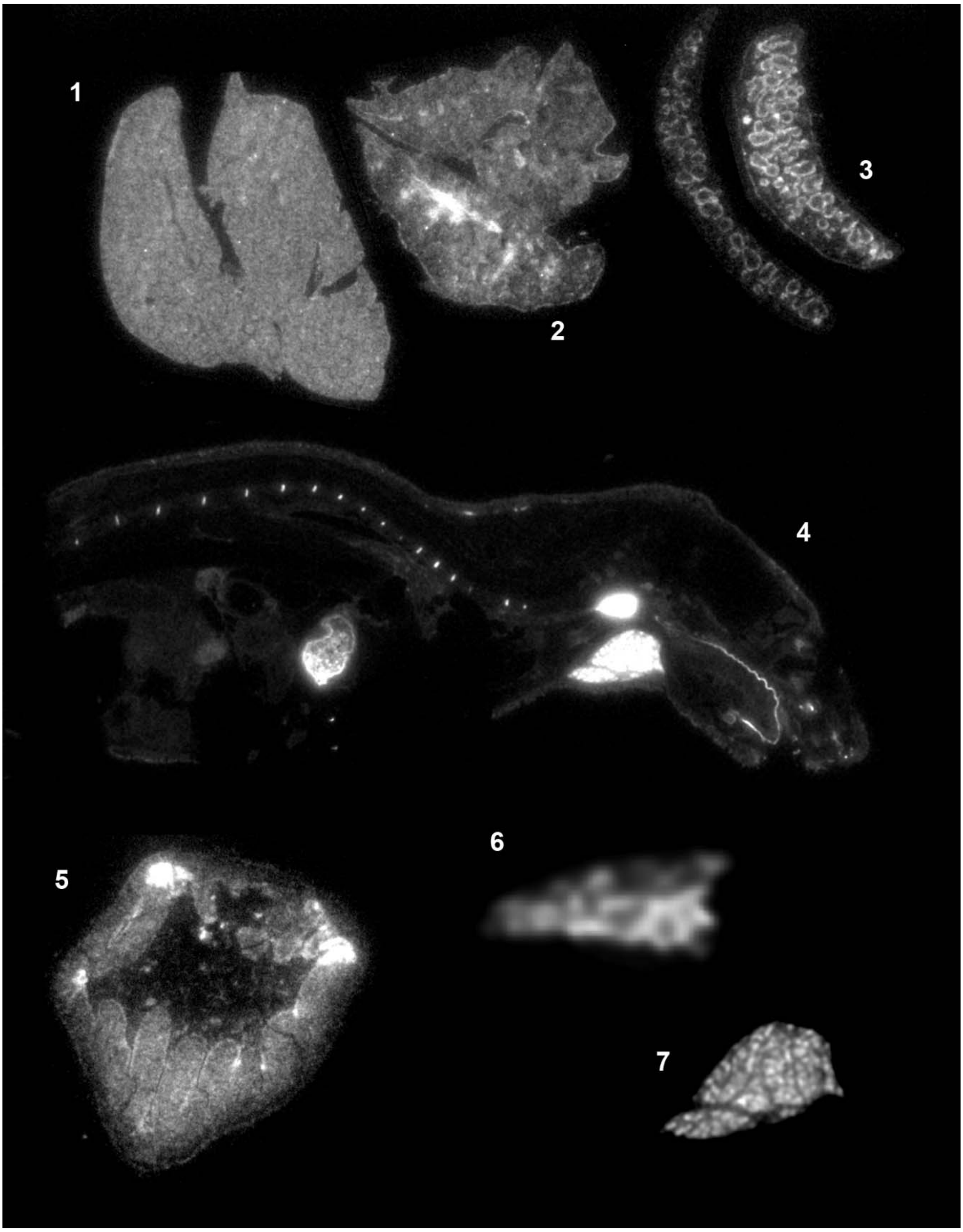

FIGURE 21. Examples of α-camera images of different normal tissues after injection of ^{211}At-IgG or free ^{211}At in mice. Section 4 -7 is the activity distribution 30 minutes after injection of free ^{211}At in a whole body section (4), the stomach (5) and blow ups from the whole body section (4) of the thyroid (6) and the salivary gland (7). Whole body-sectioning was performed by kind help Karin Hallbäck and Roland D'Argy at Active Biotech, Lund, Sweden. The sections were 10-12 μm thick.

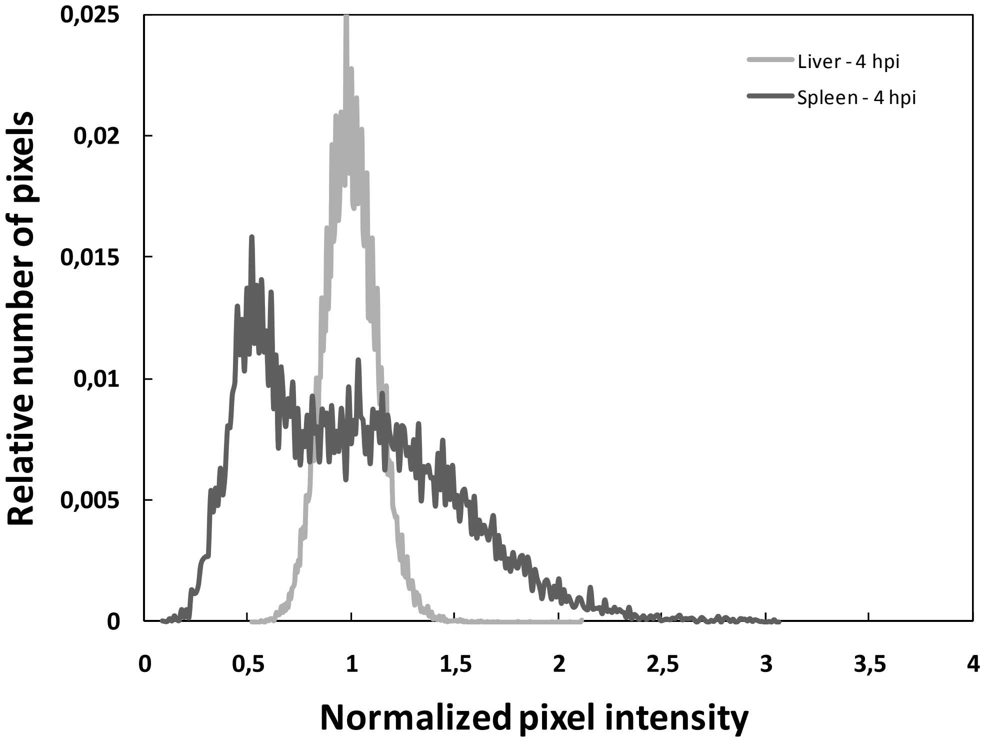

FIGURE 22. Histograms of the activity distribution of ^{211}At-IgG (MAb 1F5 at 4 hpi) in the liver and the spleen from the images in Figure X. The histograms were derived from ROIs encompassing the whole areas of the liver-section (1) and the spleen-section (3) in Figure X. The binned (256 bins) pixel intensities were normalized to the mean pixel intensity for the ROI and plotted versus the relative area (to total number of pixels in ROI).

5.4. Summary of Paper III

The α-camera was shown to have several important characteristics, all of which makes this imaging system an attractive tool to assist in the evaluation and development of targeted α-therapy. The pixel signal in the acquired images is linear to activity in the imaged object. The spatial resolution approaches the near-cellular scale and the uniformity of the detector system is good. The financial costs to set up a α-camera system are low and the imaging procedure is relatively fast.

There are several examples of important applications of the α-camera. First of all, it can visualize and quantify the time-dependent activity distributions of an α-particle emitting radionuclide in normal tissues and tumors by serial imaging of tissue sections. This means that (1); it is a tool to asses input data for small-scale dosimetry and (2) it can identify situations of nonuniform activity distributions. From the latter, the α-camera can help deciding if small-scale dosimetry is required for a certain tissue, or if organ-level dosimetry is satisfactory. For α-particles, with their short range, the activity distribution will in many cases reflect the dose distribution very well. Thus, the α-camera can assist in the selection of optimal bioconjugates for α-therapy. As suggested from many studies, a small bioconjugate may distribute faster and more uniformly in the tumor, favoring the therapeutic outcome. But this has to be weighted with the uptake patterns in the normal tissues. For small molecules labeled with an α-emitter, the kidneys may become a dose-limiting factor decreasing the maximum tolerable activity allowed for this kind of bioconjugate.

A current limitation of the α-camera is the fact that the same tissue section cannot be used for both imaging and histological staining. Instead, the morphological identification is done from a H&E-stained consecutive section (before or after the imaged section) that is superimposed on the α-imaged section. Major morphological landmarks such as peripheral borders can be aligned in the overlay procedure. But due to small differences in the placement of the cryosections when transferred to microscopy or to the scintillator, resulting in spatial displacements, the perfect superimposition can be difficult. This problem may be solved using a software that allows spatial displacement of the histological image in the overlay procedure.

6. SUMMARY AND DISCUSSION

The results and conclusions from the different papers of this thesis very much converge and relate to each others. The observations in Paper III concerning activity distribution in tissues shed new light to the studies in Paper I and Paper II. The α-camera clearly visualized that the activity distribution following α-RIT with ^{211}At-MX35-F(ab')$_2$ is largely nonuniform both in solid tumors and kidneys, especially for the time interval during which the major part of the total absorbed dose will be delivered. Future studies with the α-camera will investigate to what extent the non-uniformity found for activity distribution also will be true for the dose distributions. Such studies will have to include imaging of serial consecutive sections so that the dose contribution from neighboring sections can be modeled and accounted for. The serial sections will have to be aligned very precisely – a procedure that should be possible although technically very challenging.

As stated about the α-emitters by Humm [118] 25 years ago in his paper on dosimetric aspects on RIT, '*the usefulness of these sources in the treatment of solid tumors rely on the uniformity of the Ab distribution through the tumor*'. Many studies have shown that neither the antibody distribution, nor the activity distribution, is typically uniform and that this is a major hindrance for successive RIT. Continuing in referring to his paper, Humm stated: '*the whole concept of calculating a single mean radiation absorbed dose might conceal fluctuations in absorbed dose, the magnitude of which although extremely difficult to calculate, could be deeply relevant to achieving a specific level cell sterilization*'. Indeed, the situation of fluctuations in absorbed dose is one of the first major conclusions that can be drawn seeing the α-camera tumor images. Although future micro- or cell-level dosimetry estimations will have to investigate the full extension and consequences of them, the non-uniformities have been clearly visualized. The results from the α-camera imaging in Paper III revealed that tumor images taken at 10 minutes, 7 hours and 21 hours showed strong differences in the intratumoral distribution of the ^{211}At-MX35-F(ab')$_2$. A more uniform activity distribution was not seen until 21 hours after injection at which time 90% of the total mean absorbed dose was delivered (estimated from the biodistribution data used for dosimetry). Because of the short path length of α-particles, this non-uniformity in the activity distribution of ^{211}At will result in a very non-uniform dose distribution. Further studies with the α-camera (unpublished data), indicate that the activity distribution as quantified from the α-images will reflect the dose rate distribution rather well. The 10 minute images visualized small areas (identified from H&E-staining as vascular compartments) with very high activity relative to the surrounding tissues. At 7 hours there was markedly higher activity concentration in ring-shaped stromal compartments, surrounding clusters of tumor cells. Later studies (unpublished data) suggest that this pattern of activity distribution is valid ranging from 3 hours to around 12 hours after injection, when approximately 70% of the total absorbed dose was delivered. Quantitative analysis of the 7-hour images (Paper III, Figure 2B) revealed that the activity concentration in the stromal compartment could be approximately 3 times higher than the mean activity concentration for the whole tumor. In contrast, major parts of the the tumor cell compartments generally were at a factor of 0.5 below the mean (Paper III, Figure 2B and 2H). If this situation would be true for a time interval when most of the dose is delivered (up to 12 hours after injection), and if the activity distribution actually reflects the dose rate distribution rather well, the mean absorbed dose to the majority of tumor cells could be a factor of 0.5 lower than the mean absorbed dose to the whole tumor volume. If it is assumed that the measured growth inhibition of the tumors reflected absorbed dose to the majority of the tumor cells, this would mean that RBE would be doubled, from 5 to 10.

Alpha-camera images of the kidneys revealed a retention of the ^{211}At-MX35-F(ab')$_2$ in the renal cortex. It is indicated from the histological sections, after overlay with the α-images, that the activity is localized in the proximal tubules. The F(ab')$_2$ is filtered to some degree and once in the tubules the bioconjugate may be subjected to catabolic degradation. Radiometals (e.g. ^{90}Y) labeled to antibody fragments have been observed to accumulate in the proximal tubules [119-123] and following degradation of the ^{211}At-MX35-F(ab')$_2$, the free ^{211}At may be accumulated due to its partly metallic characteristics. If the major fraction of the absorbed dose to the kidneys (Paper II) is confined to the cortex only it can be recalculated accordingly using the cortex-to-kidney volume ratio factor (0.69 in humans

MIRD 19[91], 0.79 for rats[124]) the dose would be 22 Gy instead of the estimated 15 Gy. If the cortex-to-whole-kidney ratios found in Paper III for activity distribution were used to represent also dose distribution, using the mean ratio found for the first 270 minutes of 1.5, the estimated dose to cortex would also be 22 Gy. By α-camera imaging, future studies might identify a specific renal compartment like the cortex, or even a specific subcompartment of the cortex (e.g. proximal tubules), for which the absorbed dose after systemic α-RIT with ^{211}At-MX35-F(ab')$_2$ could be estimated. Using a small-scale dosimetry model, the tolerable dose found in Paper II for reduction in GFR could be recalculated to this specific target compartment. Thus, this tolerable dose could be translated to other targeting agents labeled with ^{211}At. Such a small-scale dosimetry model might also be scaled to the human renal dimensions and thereby help to translate the found dose response data from mouse to man.

Many papers evaluating the promises of α-emitters state in their introduction the high cytotoxic effect of α-particles by referring to the fact that only 1 to 4-6 hits to the nucleus could inactivate a cell [74, 125-130]. This reasoning can be misleading when it comes to targeted α-therapy. Even though the probability for cell death will be very high for one single cell following for example 5 traversals of α-particles through its nucleus, such an average of number of hits will not be likely to eradicate even smaller tumor cell populations. An average of 5 hits would correspond to a wide range in the distribution of the number of hits per cell, including also a certain number of cells receiving zero hits. The number of α-particle hits needed to provide a high probability for tumor eradication has been described by Roeske and Stinchcomb [56]. They modeled different parameters like nucleus size and sensitivity of cells as well as different source-to-target geometry (decays occurring inside, on the surface or outside the cell) for 7 MeV-α-particles and estimated the number of hits needed for a certain tumor control probability (TCP). For a TCP of 0.90, according to their model[60], their results showed that at this probability a large number of hits are required to eradicate a tumor cell population. They found that even small clusters of 100 cells will require 11-65 hits. For a situation that may be representative for α-RIT, i.e. decays occurring on the cell surface (due to antibody-antigen binding), a small tumor consisting of 10^6 cells would need approximately 85 hits to be eradicated. Many of the α-camera images shown in this thesis were acquired at therapeutic, or even higher, levels of injected activities. Higher activity in the imaged section will correspond to a larger number of scintillations events building up the acquired image and thus a better signal-to-noise ratio (SNR). So far, the relation between SNR and activity in the imaged sections has not been evaluated, but is likely that in many cases the SNR will allow for filtering procedures that better define the positions of decay. This will be important for small-scale dosimetry from the α-camera images.

The concept of pretargeted radioimmunotherapy (PRIT) has been shown in many studies to be an attractive development of conventional RIT. By separating the administration of the targeting agent (e.g. antibody-streptavidin conjugate) and the radionuclide in two different steps, time is allowed for the targeting agent to reach a high tumor uptake, and a decreased uptake in normal tissues, before delivery of the radionuclide (e.g. radiolabeled biotin). This gives a gain in the therapeutic window and PRIT may be the optimal method for tumor targeting with short-lived α-emitters such as ^{213}Bi or ^{211}At, as indicated by some studies [117]. A benefit of PRIT over RIT may be that a more uniform dose distribution in the tumor could be achieved, as indicated by preliminary results from collaborative studies [131] with the research group of Oliver Press (FHCRC, Seattle, USA). This can be evaluated with the α-camera and quantitative imaging can help optimize time schedules and choice of molecules in PRIT-strategies. Successful treatment of macroscopic tumors with α-RIT might be limited by reduced perfusion in the tumors and the long diffusion distances for macromolecules such as antibodies. Using a PRIT strategy, α-emitters might have a therapeutic potential for the full range of occult disease, e.g. ranging from one up to 10^9 cells (1 cm^2).

The use of α-particles in strategies of internal RT will in many cases require a refined dosimetry and modeling. This may prove very difficult for tumors because of the typical heterogeneity in growth and morphology. But since targeted α-therapy always will be limited by toxicity, the most important dosimetry may have to address the normal tissues. And due to the less heterogenic morphology of normal tissues such dosimetry may be more realistic to achieve and validate. It is important to recognize that even when detailed enough data are at hand to build a small-scale dosimetry model, that model will not be proven useful until it has been experimentally validated in a relevant biological setting; i.e. useful to predict a certain biological outcome for a certain level of absorbed dose.

The development of molecular technology has allowed the production of engineered targeting agents that can have more favorable pharmacokinetic and targeting properties [132, 133] and with the new the technologies more cancer targets can be identified and explored. In conjunction with PRIT, these new technologies hold a great promise for the future of targeted α-therapy in the treatment of cancer.

7. ACKNOWLEDGMENTS

For a long period when I was a young boy, I wanted to sit alone in the hallway of our home playing with Lego. The hallway had no windows and could therefore be turned dark when needed, so that headlight equipped and imaginary creations I've made could light up the creative mind.

My first and warmest of thanks goes to someone who always saw this young boy, namely my principal supervisor **Lars Jacobsson**. None of the efforts that I have put into research and daily work would have been the same, nor would the results, without the support from your rewarding and everlasting interest and analytical mind. I also want to thank my second supervisor, **Ragnar Hultborn**, for always opening both your door and your scientific mind.

The warmest of thanks to all the following:
Sture Lindegren, my friend, colleague and room-mate since many years. Without your superfast and creative mind, as well as patience and impatience, the long chain from radiochemistry to radiotherapy would simply not be possible. **Elisabet Warnhammar** and **Helena Kahu** for sharing your professional and skilful technical assistance, as wells as your pleasant minds. My friends and colleagues **Stig Palm**, who I want back in Gothenburg, and **Jörgen Elgqvist** for interesting discussions in and out of work. **Agne Larsson** for initiating the α-camera project and **Magnus Båth** for always sharing his brilliant mind and contributing to the α-camera project. My other co-authors; **Håkan Andersson** for being the kindest of doctors, **Chaitanya Divgi** for interest in my work, **Holger Jensen** for joyful existential conversations over a glass, **Martin E Johansson** for showing up with helpful interest in the last minute. A special thanks to **Börje Haraldsson**, who in my eyes is the finest of representatives of the research society, by always sharing his knowledge in a very joyful and humble way. All the members of our research group; **Elin Cederkrantz** for always offering kind and calm help, **Anna Gustafsson** for interesting conversations and **Sofia Frost** for always lending a helping skilful hand, despite my lack of planning, and for discussing with me the questions of life in our weekly jogging sessions. **Bengt Johansson** and **Yvonne Josefsson** for kind help with microscopy. The charming collaborators **Karin Jennbacken** and **Karin Welén** for our joyful experiments. **Peter Bernhardt** for being such a friendly colleague. **Nicolas Chouin** for adopting the α-camera studies and for turning out to be a true friend. **Karin Hallbäck** and **Roland D'Argy** for help with the whole body sectioning. **Kecke Elmroth** for discussions of research, work and life. **Ingela Claesson**, **Ulla Delle** and all the members at the Oncology Laboratory for kind help. **Niclas Pettersson**, for help with Matlab. **Sven-Bertil Orström** for engineering and discussions of life. **Sven-Erik Strand**, **Rune Nilsson** and **Anders Örbom** for co-operative work. All the friends in the **Radiation Physics** house for making it such a nice place to work in. A special thanks to **Nancy and Oliver Press** who made my research visit in Seattle a memory for life, both for me and my family. **Nural Orgun**, **Shani Frayo**, **Aimee Kenoyer**, **Darrell Fisher**, **Steven Park**, **Jaideep Shenoi**, **John Pagel**, **Scott Wilbur** and all the members of the Press group at FHCRC for showing the greatest of hospitality. I also want to thank **Eva Forssell Aronsson** for introducing me to the research field, **Lilian Karlsson** from whom I learned experimental techniques and my friend, **Börje Karlsson**, a mentor to me when I entered the research. A posthumous thanks to **Gunilla Leser**, who I miss at work very much. And, all I forgot…

Last but not least, I want to thank my beloved family for putting up with me. **Elsa** and **Elis** for giving energy back. **Moa** and **Joel** for making me feel proud of would I do. My wife **Anna** for believing in me. Apart from keeping me and our family going in life itself, you also gave me invaluable support in my work. I don't know really, how you achieved that, given our sometimes chaotic lifestyle, but the support I felt from you, in the intense phases of work, was immense. My only explanation is our love.

8. REFERENCES

1. Pressman, D. and L. Korngold, The in vivo localization of anti-Wagner-osteogenic-sarcoma antibodies. Cancer, 1953. 6(3): p. 619-23.

2. Korngold, L. and D. Pressman, The localization of antilymphosarcoma antibodies in the Murphy lymphosarcoma of the rat. Cancer Res, 1954. 14(2): p. 96-9.

3. Eisen, H.N. and D. Pressman, The zone of localization of antibodies VIII. Some properties of the antigen responsible for the renal localization of anti-kidney serum. J Immunol, 1950. 64(6): p. 487-98.

4. Kohler, G. and C. Milstein, Continuous cultures of fused cells secreting antibody of predefined specificity. Nature, 1975. 256(5517): p. 495-7.

5. Margulies, D.H., Monoclonal antibodies: producing magic bullets by somatic cell hybridization. J Immunol, 2005. 174(5): p. 2451-2.

6. Goldenberg, D.M., et al., Radioimmunodetection of cancer with radioactive antibodies to carcinoembryonic antigen. Cancer Res, 1980. 40(8 Pt 2): p. 2984-92.

7. Goldenberg, D.M., et al., Experimental radioimmunotherapy of a xenografted human colonic tumor (GW-39) producing carcinoembryonic antigen. Cancer Res, 1981. 41(11 Pt 1): p. 4354-60.

8. Goldenberg, D.M., et al., Use of radiolabeled antibodies to carcinoembryonic antigen for the detection and localization of diverse cancers by external photoscanning. N Engl J Med, 1978. 298(25): p. 1384-6.

9. Stashenko, P., et al., Characterization of a human B lymphocyte-specific antigen. J Immunol, 1980. 125(4): p. 1678-85.

10. Nadler, L.M., et al., Serotherapy of a patient with a monoclonal antibody directed against a human lymphoma-associated antigen. Cancer Res, 1980. 40(9): p. 3147-54.

11. Nadler, L.M., et al., A monoclonal antibody defining a lymphoma-associated antigen in man. J Immunol, 1980. 125(2): p. 570-7.

12. Ibritumomab tiuxetan (Zevalin) for non-Hodgkin's lymphoma. Med Lett Drugs Ther, 2002. 44(1144): p. 101-2.

13. Iodine-131 tositumomab (bexxar) for treatment of lymphoma. Med Lett Drugs Ther, 2003. 45(1168): p. 86-7.

14. Goldenberg, D.M., Targeted therapy of cancer with radiolabeled antibodies. J Nucl Med, 2002. 43(5): p. 693-713.

15. Goldenberg, D.M., Advancing role of radiolabeled antibodies in the therapy of cancer. Cancer Immunol Immunother, 2003. 52(5): p. 281-96.

16. Goldenberg, D.M. and R.M. Sharkey, Advances in cancer therapy with radiolabeled monoclonal antibodies. Q J Nucl Med Mol Imaging, 2006. 50(4): p. 248-64.

17. Oldham, R.K. and R.O. Dillman, Monoclonal antibodies in cancer therapy: 25 years of progress. J Clin Oncol, 2008. 26(11): p. 1774-7.

18. Sharkey, R.M. and D.M. Goldenberg, Perspectives on cancer therapy with radiolabeled monoclonal antibodies. J Nucl Med, 2005. 46 Suppl 1: p. 115S-27S.

19. Jodal, L., Beta emitters and radiation protection. Acta Oncologica, 2009. 48(2): p. 308-313.

20. O'Donoghue, J.A., M. Bardies, and T.E. Wheldon, Relationships between tumor size and curability for uniformly targeted therapy with beta-emitting radionuclides. J Nucl Med, 1995. 36(10): p. 1902-9.

21. Siegel, J.A. and M.G. Stabin, Absorbed fractions for electrons and beta particles in spheres of various sizes. J Nucl Med, 1994. 35(1): p. 152-6.

22. Press, O.W. and J. Rasey, Principles of radioimmunotherapy for hematologists and oncologists. Semin Oncol, 2000. 27(6 Suppl 12): p. 62-73.

23. Persaud, R.D., Biting the magic bullet. Radiolabelled monoclonal antibodies: the next great step forward in the diagnosis and treatment of cancer? Med Hypotheses, 1988. 27(3): p. 245-51.

24. Schwartz, R.S., Paul Ehrlich's magic bullets. N Engl J Med, 2004. 350(11): p. 1079-80.

25. Strebhardt, K. and A. Ullrich, Paul Ehrlich's magic bullet concept: 100 years of progress. Nat Rev Cancer, 2008. 8(6): p. 473-80.

26. Andersson, H., et al., Astatine-211-labeled antibodies for treatment of disseminated ovarian cancer: an overview of results in an ovarian tumor model. Clin Cancer Res, 2003. 9(10 Pt 2): p. 3914S-21S.

27. Andersson, H., et al., The curative and palliative potential of the monoclonal antibody MOv18 labelled with 211At in nude mice with intraperitoneally growing ovarian cancer xenografts--a long-term study. Acta Oncol, 2000. 39(6): p. 741-5.

28. Andersson, H., et al., Radioimmunotherapy of nude mice with intraperitoneally growing ovarian cancer xenograft utilizing 211At-labelled monoclonal antibody MOv18. Anticancer Res, 2000. 20(1A): p. 459-62.

29. Andersson, H., et al., Comparison of the therapeutic efficacy of 211At- and 131I-labelled monoclonal antibody MOv18 in nude mice with intraperitoneal growth of human ovarian cancer. Anticancer Res, 2001. 21(1A): p. 409-12.

30. Elgqvist, J., et al., Alpha-radioimmunotherapy of intraperitoneally growing OVCAR-3 tumors of variable dimensions: Outcome related to measured tumor size and mean absorbed dose. J Nucl Med, 2006. 47(8): p. 1342-50.

31. Elgqvist, J., et al., Fractionated radioimmunotherapy of intraperitoneally growing ovarian cancer in nude mice with 211At-MX35 F(ab')2: therapeutic efficacy and myelotoxicity. Nucl Med Biol, 2006. 33(8): p. 1065-72.

32. Elgqvist, J., et al., Therapeutic efficacy and tumor dose estimations in radioimmunotherapy of intraperitoneally growing OVCAR-3 cells in nude mice with (211)At-labeled monoclonal antibody MX35. J Nucl Med, 2005. 46(11): p. 1907-15.

33. Elgqvist, J., et al., Administered activity and metastatic cure probability during radioimmunotherapy of ovarian cancer in nude mice with 211At-MX35 F(ab')2. Int J Radiat Oncol Biol Phys, 2006. 66(4): p. 1228-37.

34. Elgqvist, J., et al., Myelotoxicity and RBE of 211At-conjugated monoclonal antibodies compared with 99mTc-conjugated monoclonal antibodies and 60Co irradiation in nude mice. J Nucl Med, 2005. 46(3): p. 464-71.

35. Andersson, H., et al., Intraperitoneal alpha-particle radioimmunotherapy of ovarian cancer patients: pharmacokinetics and dosimetry of (211)At-MX35 F(ab')2--a phase I study. J Nucl Med, 2009. 50(7): p. 1153-60.

36. Jurcic, J.G., et al., Targeted alpha particle immunotherapy for myeloid leukemia. Blood, 2002. 100(4): p. 1233-9.

37. Rosenblat, T.L., et al., Sequential cytarabine and alpha-particle immunotherapy with bismuth-213-lintuzumab (HuM195) for acute myeloid leukemia. Clin Cancer Res, 2010. 16(21): p. 5303-11.

38. Rosenblat, T.L., et al., Phase I Trial of the Targeted Alpha-Particle Nano-Generator Actinium-225 (225Ac)-HuM195 (Anti-CD33) in Acute Myeloid Leukemia (AML). ASH Annual Meeting Abstracts, 2007. 110(11): p. 910-.

39. Zalutsky, M.R., et al., Clinical experience with alpha-particle emitting 211At: treatment of recurrent brain tumor patients with 211At-labeled chimeric antitenascin monoclonal antibody 81C6. J Nucl Med, 2008. 49(1): p. 30-8.

40. Nilsson, S., et al., Bone-targeted radium-223 in symptomatic, hormone-refractory prostate cancer: a randomised, multicentre, placebo-controlled phase II study. Lancet Oncol, 2007. 8(7): p. 587-94.

41. Wilbur, D.S., et al., Preparation and evaluation of para-[211At]astatobenzoyl labeled anti-renal cell carcinoma antibody A6H F(ab')2. In vivo distribution comparison with para-[125I]iodobenzoyl labeled A6H F(ab')2. Nucl Med Biol, 1993. 20(8): p. 917-27.

42. Lindegren, S., T. Back, and H.J. Jensen, Dry-distillation of astatine-211 from irradiated bismuth targets: a time-saving procedure with high recovery yields. Appl Radiat Isot, 2001. 55(2): p. 157-60.

43. Lindegren, S., et al., High-efficiency astatination of antibodies using N-iodosuccinimide as the oxidising agent in labelling of N-succinimidyl 3-(trimethylstannyl)benzoate. Nucl Med Biol, 2001. 28(1): p. 33-9.

44. Lindegren, S., et al., Direct procedure for the production of 211At-labeled antibodies with an epsilon-lysyl-3-(trimethylstannyl)benzamide immunoconjugate. J Nucl Med, 2008. 49(9): p. 1537-45.

45. Howell, R.W., S.M. Goddu, and D.V. Rao, Application of the linear-quadratic model to radioimmunotherapy: further support for the advantage of longer-lived radionuclides. J Nucl Med, 1994. 35(11): p. 1861-9.

46. Dale, R., Use of the linear-quadratic radiobiological model for quantifying kidney response in targeted radiotherapy. Cancer Biother Radiopharm, 2004. 19(3): p. 363-70.

47. Bentzen, S.M., Preventing or reducing late side effects of radiation therapy: radiobiology meets molecular pathology. Nat Rev Cancer, 2006. 6(9): p. 702-13.

48. Prise, K.M., et al., New insights on cell death from radiation exposure. Lancet Oncol, 2005. 6(7): p. 520-8.

49. Stewart, F.A. and W. Dorr, Milestones in normal tissue radiation biology over the past 50 years: from clonogenic cell survival to cytokine networks and back to stem cell recovery. Int J Radiat Biol, 2009. 85(7): p. 574-86.

50. Roeske, J.C., et al., Small-scale dosimetry: challenges and future directions. Semin Nucl Med, 2008. 38(5): p. 367-83.

51. Humm, J.L., et al., MICRODOSIMETRY IN RADIOIMMUNOTHERAPY. Radiation Protection Dosimetry, 1990. 31(1-4): p. 433-436.

52. Kassis, A.I., Radiotargeting agents for cancer therapy. Expert Opin Drug Deliv, 2005. 2(6): p. 981-91.

53. Sgouros, G., Alpha-particles for targeted therapy. Adv Drug Deliv Rev, 2008. 60(12): p. 1402-6.

54. Sgouros, G., et al., MIRD Pamphlet No. 22 (abridged): radiobiology and dosimetry of alpha-particle emitters for targeted radionuclide therapy. J Nucl Med, 2010. 51(2): p. 311-28.

55. Roeske, J.C. and T.G. Stinchcomb, Relationships between cell survival and specific energy spectra for therapeutic alpha-particle emitters. Radiat Res, 1996. 145(3): p. 268-73.

56. Roeske, J.C. and T.G. Stinchcomb, The average number of alpha-particle hits to the cell nucleus required to eradicate a tumour cell population. Phys Med Biol, 2006. 51(9): p. N179-86.

57. Humm, J.L., A microdosimetric model of astatine-211 labeled antibodies for radioimmunotherapy. Int J Radiat Oncol Biol Phys, 1987. 13(11): p. 1767-73.

58. Humm, J.L., et al., Microdosimetric concepts in radioimmunotherapy. Med Phys, 1993. 20(2 Pt 2): p. 535-41.

59. Roeske, J.C. and T.G. Stinchcomb, Dosimetric framework for therapeutic alpha-particle emitters. J Nucl Med, 1997. 38(12): p. 1923-9.

60. Roeske, J.C. and T.G. Stinchcomb, Tumor control probability model for alpha-particle-emitting radionuclides. Radiat Res, 2000. 153(1): p. 16-22.

61. Stinchcomb, T.G. and J.C. Roeske, Values of "S," <z1>, and <(z1)2> for dosimetry using alpha-particle emitters. Med Phys, 1999. 26(9): p. 1960-71.

62. Goddu, S.M., R.W. Howell, and D.V. Rao, Cellular dosimetry: absorbed fractions for monoenergetic electron and alpha particle sources and S-values for radionuclides uniformly distributed in different cell compartments. J Nucl Med, 1994. 35(2): p. 303-16.

63. Hall, E., Radiobiology for the radiologist.

64. Hall, E.J., et al., SURVIVAL CURVES AND AGE RESPONSE FUNCTIONS FOR CHINESE-HAMSTER CELLS EXPOSED TO X-RAYS OR HIGH LET ALPHA-PARTICLES. Radiation Research, 1972. 52(1): p. 88-&.

65. Cox, R., et al., Mutation and inactivation of mammalian cells by various ionising radiations. Nature, 1977. 267(5610): p. 425-7.

66. Claesson, K., et al., RBE of -particles from (211)At for complex DNA damage and cell survival in relation to cell cycle positio. Int J Radiat Biol, 2010.

67. Humm, J.L. and L.M. Chin, A model of cell inactivation by alpha-particle internal emitters. Radiat Res, 1993. 134(2): p. 143-50.

68. Fisher, D.R., M.E. Frazier, and T.K. Andrews, ENERGY-DISTRIBUTION AND THE RELATIVE BIOLOGICAL EFFECTS OF INTERNAL ALPHA EMITTERS. Radiation Protection Dosimetry, 1985. 13(1-4): p. 223-227.

69. Neti, P.V. and R.W. Howell, Log normal distribution of cellular uptake of radioactivity: implications for biologic responses to radiopharmaceuticals. J Nucl Med, 2006. 47(6): p. 1049-58.

70. Neti, P.V. and R.W. Howell, Lognormal distribution of cellular uptake of radioactivity: statistical analysis of alpha-particle track autoradiography. J Nucl Med, 2008. 49(6): p. 1009-16.

71. Kvinnsland, Y., T. Stokke, and E. Aurlien, Radioimmunotherapy with alpha-particle emitters: microdosimetry of cells with a heterogeneous antigen expression and with various diameters of cells and nuclei. Radiat Res, 2001. 155(2): p. 288-96.

72. Kvinnsland, Y., T. Stokke, and E. Aurlien, Log normal distribution of cellular uptake of radioactivity. J Nucl Med, 2007. 48(2): p. 327; author reply 327-8.

73. Palm, S., et al., In vitro effects of free 211At,211At-albumin and 211At-monoclonal antibody compared to external photon irradiation on two human cancer cell lines. Anticancer Res, 2000. 20(2A): p. 1005-12.

74. Kassis, A.I., et al., The in vitro radiobiology of astatine-211 decay. Radiat Res, 1986. 105(1): p. 27-36.

75. Claesson, A.K., et al., Relative biological effectiveness of the alpha-particle emitter (211)At for double-strand break induction in human fibroblasts. Radiat Res, 2007. 167(3): p. 312-8.

76. Akabani, G., et al., In vitro cytotoxicity of 211At-labeled trastuzumab in human breast cancer cell lines: effect of specific activity and HER2 receptor heterogeneity on survival fraction. Nucl Med Biol, 2006. 33(3): p. 333-47.

77. Vandenbulcke, K., et al., In vitro evaluation of 213Bi-rituximab versus external gamma irradiation for the treatment of B-CLL patients: relative biological efficacy with respect to apoptosis induction and chromosomal damage. Eur J Nucl Med Mol Imaging, 2003. 30(10): p. 1357-64.

78. Dahle, J., et al., In vitro cytotoxicity of low-dose-rate radioimmunotherapy by the alpha-emitting radioimmunoconjugate Thorium-227-DOTA-rituximab. Int J Radiat Oncol Biol Phys, 2009. 75(3): p. 886-95.

79. Heyerdahl, H., et al., Treatment of HER2-expressing breast cancer and ovarian cancer cells with alpha particle-emitting 227Th-trastuzumab. Int J Radiat Oncol Biol Phys, 2011. 79(2): p. 563-70.

80. Harrison, A. and L. Royle, Determination of absorbed dose to blood, kidneys, testes and thyroid in mice injected with 211At and comparison of testes mass and sperm number in x-irradiated and 211At treated mice. Health Phys, 1984. 46(2): p. 377-83.

81. Howell, R.W., et al., Relative biological effectiveness of alpha-particle emitters in vivo at low doses. Radiat Res, 1994. 137(3): p. 352-60.

82. Howell, R.W., et al., Radiotoxicity of gadolinium-148 and radium-223 in mouse testes: relative biological effectiveness of alpha-particle emitters in vivo. Radiat Res, 1997. 147(3): p. 342-8.

83. Dahle, J., O.S. Bruland, and R.H. Larsen, Relative biologic effects of low-dose-rate alpha-emitting 227Th-rituximab and beta-emitting 90Y-tiuexetan-ibritumomab versus external beam X-radiation. Int J Radiat Oncol Biol Phys, 2008. 72(1): p. 186-92.

84. Behr, T.M., et al., High-linear energy transfer (LET) alpha versus low-LET beta emitters in radioimmunotherapy of solid tumors: therapeutic efficacy and dose-limiting toxicity of 213Bi- versus 90Y-labeled CO17-1A Fab' fragments in a human colonic cancer model. Cancer Res, 1999. 59(11): p. 2635-43.

85. Back, T., et al., 211At radioimmunotherapy of subcutaneous human ovarian cancer xenografts: evaluation of relative biologic effectiveness of an alpha-emitter in vivo. J Nucl Med, 2005. 46(12): p. 2061-7.

86. Nadasdy, T., et al., Proliferative activity of intrinsic cell populations in the normal human kidney. J Am Soc Nephrol, 1994. 4(12): p. 2032-9.

87. Cybulla, M., S.M. Weiner, and A. Otte, End-stage renal disease after treatment with 90Y-DOTATOC. Eur J Nucl Med, 2001. 28(10): p. 1552-4.

88. Valkema, R., et al., Long-term follow-up of renal function after peptide receptor radiation therapy with (90)Y-DOTA(0),Tyr(3)-octreotide and (177)Lu-DOTA(0), Tyr(3)-octreotate. J Nucl Med, 2005. 46 Suppl 1: p. 83S-91S.

89. Konijnenberg, M., et al., Radiation dose distribution in human kidneys by octreotides in peptide receptor radionuclide therapy. J Nucl Med, 2007. 48(1): p. 134-42.

90. Wessels, B.W., et al., MIRD Pamphlet No. 20: The Effect of Model Assumptions on Kidney Dosimetry and Response--Implications for Radionuclide Therapy. J Nucl Med, 2008.

91. Bouchet, L.G., et al., MIRD Pamphlet No 19: absorbed fractions and radionuclide S values for six age-dependent multiregion models of the kidney. J Nucl Med, 2003. 44(7): p. 1113-47.

92. Haraldsson, B. and B. Rippe, Upper and lower bounds on capillary permeability ratios of Cr-EDTA to cyanocobalamin in rat hindquarters. Acta Physiol Scand, 1991. 143(3): p. 239-41.

93. Guo, L., et al., Denaturant-induced expansion and compaction of a multi-domain protein: IgG. J Mol Biol, 2008. 384(5): p. 1029-36.

94. Armstrong, J.K., et al., The hydrodynamic radii of macromolecules and their effect on red blood cell aggregation. Biophys J, 2004. 87(6): p. 4259-70.

95. Haraldsson, B., J. Nystrom, and W.M. Deen, Properties of the glomerular barrier and mechanisms of proteinuria. Physiol Rev, 2008. 88(2): p. 451-87.

96. Birn, H. and E.I. Christensen, Renal albumin absorption in physiology and pathology. Kidney Int, 2006. 69(3): p. 440-9.

97. Birn, H., et al., Megalin is essential for renal proximal tubule reabsorption and accumulation of transcobalamin-B(12). Am J Physiol Renal Physiol, 2002. 282(3): p. F408-16.

98. de Jong, M., et al., Megalin is essential for renal proximal tubule reabsorption of (111)In-DTPA-octreotide. J Nucl Med, 2005. 46(10): p. 1696-700.

99. Schwartz, G.J. and S.L. Furth, Glomerular filtration rate measurement and estimation in chronic kidney disease. Pediatr Nephrol, 2007. 22(11): p. 1839-48.

100. Addis, T., B. Myers, and J. Oliver, The regulation of renal activity. IX. The effect of unilateral nephrectomy on the function and structure of the remaining kidney. Archives of Internal Medicine, 1924(34): p. 243-57.

101. Messow, C., et al., Sex differences in kidney morphology and glomerular filtration rate in mice. Contrib Nephrol, 1980. 19: p. 51-5.

102. Qi, Z., et al., Serial determination of glomerular filtration rate in conscious mice using FITC-inulin clearance. Am J Physiol Renal Physiol, 2004. 286(3): p. F590-6.

103. Thomas, C. and L. Thomas, Renal failure--measuring the glomerular filtration rate. Dtsch Arztebl Int, 2009. 106(51-52): p. 849-54.

104. Jaggi, J.S., et al., Renal tubulointerstitial changes after internal irradiation with alpha-particle-emitting actinium daughters. J Am Soc Nephrol, 2005. 16(9): p. 2677-89.

105. Wiesli, P., et al., Serum cystatin C is sensitive to small changes in thyroid function. Clin Chim Acta, 2003. 338(1-2): p. 87-90.

106. Emami, B., et al., Tolerance of normal tissue to therapeutic irradiation. Int J Radiat Oncol Biol Phys, 1991. 21(1): p. 109-22.

107. Humm, J.L., et al., Internal dosimetry using data derived from autoradiographs. J Nucl Med, 1993. 34(10): p. 1811-7.

108. Akabani, G., S.J. Kennel, and M.R. Zalutsky, Microdosimetric analysis of alpha-particle-emitting targeted radiotherapeutics using histological images. J Nucl Med, 2003. 44(5): p. 792-805.

109. Brown, I., R.N. Carpenter, and J.S. Mitchell, The development of A [211At]-astatinated endoradiotherapeutic drug: Part I. Localization by alpha-particle autoradiography in a murine tumor model. Int J Radiat Oncol Biol Phys, 1992. 23(3): p. 563-72.

110. Larsen, R.H. and O.S. Bruland, Intratumour injection of immunoglobulins labelled with the alpha-particle emitter 211At: analyses of tumour retention, microdistribution and growth delay. Br J Cancer, 1998. 77(7): p. 1115-22.

111. Hassfjell, S., K. Ingebrigtsen, and O.S. Bruland, Synthesis, purification and biodistribution of (205)Bi-DOTMP, visualizing bone deposition patterns with autoradiography. Nucl Med Biol, 2001. 28(4): p. 425-33.

112. Dahle, J., et al., Assessment of long-term radiotoxicity after treatment with the low-dose-rate alpha-particle-emitting radioimmunoconjugate (227)Th-rituximab. Eur J Nucl Med Mol Imaging, 2010. 37(1): p. 93-102.

113. Kolar, Z.I. and W. Den Hollander, 2003: a centennial of spinthariscope and scintillation counting. Appl Radiat Isot, 2004. 61(2-3): p. 261-6.

114. Wood, R.W., The scintillations of radium. Science, 1904. 29(19): p. 195-196.

115. Wood, R.W., A Fire-Fly "Spinthariscope". Science, 1939. 90(2332): p. 233-234.

116. Thurber, G.M., M.M. Schmidt, and K.D. Wittrup, Factors determining antibody distribution in tumors. Trends Pharmacol Sci, 2008. 29(2): p. 57-61.

117. Park, S.I., et al., Conventional and pretargeted radioimmunotherapy using bismuth-213 to target and treat non-Hodgkin lymphomas expressing CD20: a preclinical model toward optimal consolidation therapy to eradicate minimal residual disease. Blood, 2010. 116(20): p. 4231-9.

118. Humm, J.L., Dosimetric aspects of radiolabeled antibodies for tumor therapy. J Nucl Med, 1986. 27(9): p. 1490-7.

119. Casey, J.L., et al., Preparation, characterisation and tumour targeting of cross-linked divalent and trivalent anti-tumour Fab' fragments. Br J Cancer, 1996. 74(9): p. 1397-405.

120. King, D.J., et al., Improved tumor targeting with chemically cross-linked recombinant antibody fragments. Cancer Res, 1994. 54(23): p. 6176-85.

121. Sharkey, R.M., et al., Biodistribution and radiation dose estimates for yttrium- and iodine-labeled monoclonal antibody IgG and fragments in nude mice bearing human colonic tumor xenografts. Cancer Res, 1990. 50(8): p. 2330-6.

122. Schott, M.E., et al., Differential metabolic patterns of iodinated versus radiometal chelated anticarcinoma single-chain Fv molecules. Cancer Res, 1992. 52(22): p. 6413-7.

123. Flynn, A.A., et al., The nonuniformity of antibody distribution in the kidney and its influence on dosimetry. Radiat Res, 2003. 159(2): p. 182-9.

124. Altunkaynak, M.E., et al., The effects of high-fat diet on the renal structure and morphometric parametric of kidneys in rats. J Anat, 2008. 212(6): p. 845-52.

125. Charlton, D.E., A.I. Kassis, and S.J. Adelstein, A COMPARISON OF EXPERIMENTAL AND CALCULATED SURVIVAL CURVES FOR V79 CELLS GROWN AS MONOLAYERS OR IN SUSPENSION EXPOSED TO ALPHA-IRRADIATION FROM BI-212 DISTRIBUTED IN THE GROWTH-MEDIUM. Radiation Protection Dosimetry, 1994. 52(1-4): p. 311-315.

126. Walicka, M.A., et al., Survival and DNA damage in Chinese hamster V79 cells exposed to alpha particles emitted by DNA-incorporated astatine-211. Radiat Res, 1998. 150(3): p. 263-8.

127. Bird, R.P., et al., Inactivation of synchronized Chinese Hamster V79 cells with charged-particle track segments. Radiat Res, 1980. 82(2): p. 277-89.

128. Raju, M.R., et al., Radiobiology of alpha particles. III. Cell inactivation by alpha-particle traversals of the cell nucleus. Radiat Res, 1991. 128(2): p. 204-9.

129. Roberts, C.J. and D.T. Goodhead, The effect of 238Pu alpha-particles on the mouse fibroblast cell line C3H 10T1/2: characterization of source and RBE for cell survival. Int J Radiat Biol Relat Stud Phys Chem Med, 1987. 52(6): p. 871-82.

130. Todd, P., et al., Lethal, potentially lethal, and nonlethal damage induction by heavy ions in cultured human cells. Radiat Res Suppl, 1985. 8: p. S5-12.

131. Kenoyer, A.L., et al., Anti-CD45 Ab Pretargeted Radioimmunotherapy Using An Alpha Emitting Radionuclide (213Bi) Delivers Selective Radiation to Human Myeloid Leukemias in a Mouse Xenograft Model and Results in High Rates of Complete Remission and Long Term Survival. ASH Annual Meeting Abstracts, 2009. 114(22): p. 1035-.

132. Dearling, J.L. and R.B. Pedley, Technological advances in radioimmunotherapy. Clin Oncol (R Coll Radiol), 2007. 19(6): p. 457-69.

133. Sharkey, R.M. and D.M. Goldenberg, Advances in radioimmunotherapy in the age of molecular engineering and pretargeting. Cancer Invest, 2006. 24(1): p. 82-97.